Weierstraß-Institut
für Angewandte Analysis und Stochastik

Leibniz-Institut im Forschungsverbund Berlin e. V.

Preprint ISSN 2198-5855

Numerical upscaling of parametric microstructures in a possibilistic uncertainty framework with tensor trains

Martin Eigel[1], Robert Gruhlke[1], Dieter Moser[2]

submitted: December 22, 2021

[1] Weierstrass Institute
Mohrenstr. 39
10117 Berlin
Germany
E-Mail: robert.gruhlke@wias-berlin.de
martin.eigel@wias-berlin.de

[2] Institut für Geometrie und Praktische Mathematik
RWTH Aachen
Templergraben 55
52056 Aachen
Germany
E-Mail: moser@igpm.rwth-aachen.de

No. 2907
Berlin 2021

2020 *Mathematics Subject Classification.* 15A69, 35R13, 65N12, 65N22, 65J10, 74B05, 97N50.

Key words and phrases. Fuzzy partial differential equations, possibility, polymorphic uncertainty modeling, uncertainty quantification, low-rank hierarchical tensor formats, parametric partial differential equations, linear elasticity, homogenisation, tensor trains.

The authors acknowledge the support by the DFG SPP1886 “Polymorphic uncertainty modelling for the numerical design of structures“.

Edited by
Weierstraß-Institut für Angewandte Analysis und Stochastik (WIAS)
Leibniz-Institut im Forschungsverbund Berlin e. V.
Mohrenstraße 39
10117 Berlin
Germany

Fax: +49 30 20372-303
E-Mail: preprint@wias-berlin.de
World Wide Web: http://www.wias-berlin.de/

Numerical upscaling of parametric microstructures in a possibilistic uncertainty framework with tensor trains

Martin Eigel, Robert Gruhlke, Dieter Moser

Abstract

A fuzzy arithmetic framework for the efficient possibilistic propagation of shape uncertainties based on a novel fuzzy edge detection method is introduced. The shape uncertainties stem from a blurred image that encodes the distribution of two phases in a composite material. The proposed framework employs computational homogenisation to upscale the shape uncertainty to a fuzzy effective material. For this, many samples of a linear elasticity problem have to be computed, which is significantly sped up by a highly accurate low-rank tensor surrogate. To ensure the continuity of the underlying mapping from shape parametrisation to the upscaled material behaviour, a diffeomorphism is constructed by generating an appropriate family of meshes via transformation of a reference mesh. The shape uncertainty is then propagated to measure the distance of the upscaled material to the isotropic and orthotropic material class. Finally, the fuzzy effective material is used to compute bounds for the average displacement of a non-homogenized material with uncertain star-shaped inclusion shapes.

1 Introduction

Composite materials are ubiquitous in many applications. Whether they are formed by chance (like with unfavourable impurities in metal) or by design (like pebbles in concrete), the mechanical properties of the whole material are determined by the resulting composite structure [27]. The different types of composite materials – *e.g.* metal matrix composites [12], fiber-reinforced polymers [52], composite wood [41] and other advanced composite materials [56] – find their use in a wide range of applications, e.g. masonry, aerospace industry, wind power plants and sports equipment. In many applications, the added composite material improves a base matrix material in terms of wear resistance, damping properties and mechanical strength, while keeping the same weight. However, such improved composite materials are a result of empirical studies, experimentation and chance. It hence is obvious that a thorough understanding of composite materials via theoretical and accurate computational models is desirable to predict and systematically improve the properties and applicability of composites.

What makes this task challenging are the influence of material behaviour on the *micro- and macro scales*, as well as the multifaceted sources of *uncertainties*. For instance, the involved length scales may span up to ten orders of magnitudes, i.e. the size of a nano particle of $10^{-6}\,\mathrm{m}$ is embedded in a material with a length scale of $10^{-1} - 10^{1}\,\mathrm{m}$ [12]. The same holds for the material constants if the constituents are fundamentally different as in metals and polymers. A standard finite element approach becomes very costly in such a setting since the details of the composite have to be resolved by the mesh for accurate simulations. Additionally, one has to handle the uncertainty of the material constants such as the position, form and size of the inclusions. This increases the costs even further since many realisations are required to correctly capture the uncertainty statistically. Each new realisations requires a costly (possible automatic) remeshing of the computational domain. The mapping from

DOI 10.20347/WIAS.PREPRINT.2907 Berlin 2021

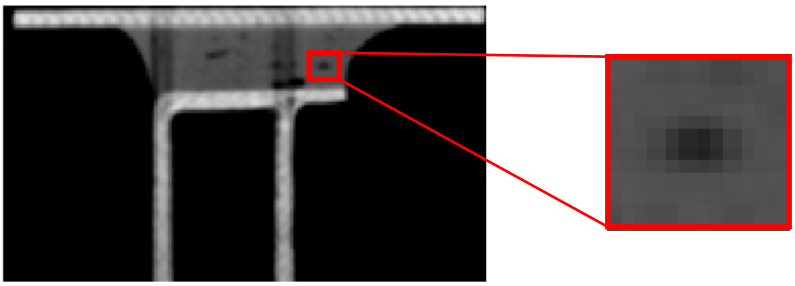

Figure 1: Computed tomography scan of a Henkel beam taken from [15]. Material imperfections are noticeable but the present resolution does not reveal the exact shapes of the imperfections.

geometric parameters — namely position and shape of each inclusion — onto the generated meshes are usually discontinuous. This introduces unwanted effects that we tackle in Section 4.1.

The first challenge — the span of scales — is tackled by *homogenisation* methods, a term introduced by Babuška in [3]. In some form or another, these methods incorporate micro-scale behaviour into an adjusted macro-scale model, replacing the full composite material model by a corrected homogeneous one, obtained by an asymptotic limit of an assumed (periodic) domain. The central idea is to derive equations that describe the effective material properties analytically. Alternatively, computational approaches have been devised to solve particular micro-scale problems to deduce the adjusted macro-scale behaviour numerically [10, 19]. Some notable examples are stochastic homogenisation, see [1, 7, 8, 22], projection based homogenisation [18] and (stochastic) representative volume element methods [43].

The second challenge — the uncertainty of the material — is sometimes neglected [29, 55] by only considering deterministic material properties. If the probability distribution of the material constants is known, the uncertainty can be modelled with *precise probabilities* [4]. Ignoring the uncertainty seems valid if it has little influence on the system's response or the model data is known sufficiently accurate and is free of inherent fluctuations. Using precise probabilities is valid if the distributions of the material constants are known precisely. However, as was pointed out by Motamed and Babuška [5], stochastic models based on precise probabilities are not always able to model the uncertainty in composite materials. Instead, they propose a model based on an imprecise probability theory. Examples for this are evidence theory [53], random set theory [34], possibility theory [61] and — more recently — optimal Uncertainty Quantification (UQ) [45]. In comparison to precise probability, imprecise probability methods are able to provide estimates of uncertainties based only on a small set of data and few assumptions, which would be far too limited for a probabilistic method. For an illuminating work that dissects the difference between precise and imprecise probabilities, we refer the reader to [6]. As a motivation the approach developed in what follows, we especially point to the *false confidence theorem*, which qualitatively states that "probability dilution is a symptom of a fundamental deficiency in probabilistic representations of statistical inference, in which there are propositions that will consistently be assigned a high degree of belief, regardless of whether or not they are true" [6].

In this work, we consider a practical problem that is supposed to illustrate when imprecise probabilities are appropriate (in particular more so than probabilistic methods), the challenges performing a non-probabilistic uncertainty propagation and quantification, and ways to overcome the computational difficulties. We assume a material consisting of two phases, namely a soft matrix phase and a hard inclusion phase. Both phases are linear elastic with precisely known Young's modulus and Poisson ratio. The inclusions repeat periodically in a checkerboard fashion. Consequently, a classical numerical homogenisation method would yield a homogenised (globally constant) macro-scale material. Consid-

ering real applications, the main problem stems from the unknown shape of the inclusions. Often, the shape is retrieved with a non-intrusive imaging process, e.g. computed tomography scans or magnetic resonance imaging. To illustrate this, Figure 1 shows a computed tomography scan of an imperfect adhesive bond within a Henkel beam, cf. [15]. Apparently, the image is noisy, blurred, pixelated and exhibits artefacts. While it is possible to *de-noise* and *de-blurr* the image with image post-processing, which might make the identification of inclusions possible, different numerical methods yield different shapes [16]. This reveals the shape uncertainty inherent to the image. Here, we just focus on blurred images, assuming that the artefacts and noise were successfully removed already, see Figure 3 for an example.

To tackle this setting, we introduce a novel *fuzzy edge detection* based on possibility theory, presented in Section 2.1 and a restriction of possible interface boundaries via bounded total variation in Section 3. This yields a fuzzy model of the boundary which in turn introduces a computational challenge in terms of a numerical homogenisation problem as discussed in Section 2.2. For this, the micro-model has to be solved very often in order to propagate the uncertainty of the boundary to the homogenised material model. To alleviate this expensive task, we introduce a highly accurate rank adaptive low-rank tensor surrogate in Section 4. In the numerical experiments Section 5, the surrogate model is validated numerically. Moreover, we measure the distance of the homogenised material to the class of isotropic and orthotropic elastic tensors and eventually use the homogenised material to perform a worst/best case analysis for a full matrix composite model with 64 inclusions, i.e., with help of the homogenised material we will find bounds for the average displacement of the non-homogenised material.

2 Basics

This section serves as a brief introduction of three fundamental topics that form the basis of this work. First, *fuzzy set theory* which is used to model the uncertainty ingrained in the blurred image. Second, the *computational up-scaling* method (numerical homogenisation). Third, classes of *constitutive tensors* to measure the distance of the up-scaled material to the isotropic and orthotropic material are discussed.

2.1 Fuzzy set theory

We introduce a *possibilistic framework* with fuzzy sets based on 4 central definitions, see e.g. [60] or more recently [36, 37, 38]. Fuzzy sets are common sets that are equipped with a *membership function* which assigns each element in the set a value between zero and one. This values only task is to communicate a *degree of belongingness* to the set. The meaning of this value depends on the problem and — more importantly — on the community using this value to formalise uncertainty. Arguably, this ambiguity is a feature and not a short-coming of this theory since it avoids assumptions that are usually made by other approaches. In probability theory for instance, one has to assume a prior distribution before updating the posterior distribution with new samples.

The following definition introduces the terminology of fuzzy sets.

Definition 2.1. ***(Fuzzy set/variable, α-cuts and interactivity)***
Let $Z \neq \emptyset$ be a set and $\mu\colon Z \to [0,1]$ be a map such that there exists $z \in Z$ with $\mu(z) = 1$. The map μ is called (normalised) membership function. We define a (normalised) fuzzy set $\tilde{z}$ on Z by

$$\tilde{z} := \{(z, \mu(z)) \,|\, z \in Z\}. \tag{1}$$

If $\mu(Z) = \{0,1\}$ with unique $z^* \in Z$ and $\mu(z^*) = 1$ then $\tilde{z}$ is called a crisp set. Furthermore, we denote by $\mathcal{F}(Z)$ the set of all fuzzy sets on Z. We thus simply write $\tilde{z} \in \mathcal{F}(Z)$. For each fuzzy set $\tilde{z} \in \mathcal{F}(Z)$ we denote the associated membership function by $\mu_{\tilde{z}}$. If $Z \subset \mathbb{R}^N$ for $N \in \mathbb{N}$, we call $\tilde{z} \in \mathcal{F}(Z)$ a fuzzy variable $(N = 1)$ or vectorial fuzzy variable $(N > 1)$ described by a (joint) membership function $\mu_{\tilde{z}}$. Let $\alpha \in [0,1]$. Then the α-cut C_α of $\mu_{\tilde{z}}$ is defined as

$$C_\alpha[\tilde{z}] := \{z \in Z : \mu_{\tilde{z}}(z) \geq \alpha\}. \tag{2}$$

The support of $\mu_{\tilde{z}}$ is defined as

$$\operatorname{supp}(\tilde{z}) = \{z \in Z \mid \mu_{\tilde{z}}(z) > 0\}.$$

Let $\tilde{z}_i \in \mathcal{F}(Z_i)$ for sets Z_i with $i = 1, \dots, M < \infty$, $Z := \bigtimes_{i=1}^M Z_i$ and $\tilde{z} = (\tilde{z}_1, \dots, \tilde{z}_M)$. If the joint membership function associated with $\tilde{z}$ has the form $\mu_{\tilde{z}} = \min_i \mu_{\tilde{z}_i}$ then $\tilde{z}$ is called non-interactive and interactive otherwise.

Fuzzy sets are quite versatile since there are no restrictions on the (type and structure of the) used sets. However, for numerical methods to become efficient, certain assumptions are beneficial. The first restriction mimics numbers and vectors.

Definition 2.2. ***(Fuzzy number/vector)***
Let $\tilde{z} \in \mathcal{F}(Z)$ with $Z \subset \mathbb{R}^N$ for some $N \in \mathbb{N}$ such that Z is bounded and convex and the (joint) membership function $\mu_{\tilde{z}}$ is upper semi-continuous, i.e.

$$\limsup_{z \to z_0} \mu(z) \leq \mu(z_0), \quad \forall z_0 \in Z \tag{3}$$

and quasi-concave, i.e.

$$\mu(\lambda z_1 + (1-\lambda) z_2) \geq \min(\mu(z_1), \mu(z_2)), \quad \forall z_1, z_2 \in Z. \tag{4}$$

If there exists a unique $z^* \in Z$ such that $\mu_{\tilde{z}}(z^*) = 1$ then we call $\tilde{z}$ a fuzzy number for $n = 1$ and a fuzzy vector for $n > 1$.

This notion is easily extended to intervals and domains.

Definition 2.3. ***(Fuzzy interval/domain)***
With the same assumptions as in Definition 2.2, there exists a subset $S \subset Z$ such that $\mu_{\tilde{z}}(z) = 1$ for all $z \in S$. Then $\tilde{z}$ is called a fuzzy interval for $n = 1$ and fuzzy domain for $n > 1$.

Note that the quasi-concavity of the membership function implies convexity of any α-cut C_α. In particular, given $S \subset Z$ as in Definition 2.3, the convex hull $\operatorname{conv}(S)$ is a proper subset of C_1, too. The quasi-concavity also leads to the nestedness property of α-cuts from Definitions 2.2 and 2.3, i.e.

$$C_\alpha[\tilde{z}] \subset C_\beta[\tilde{z}], \quad \forall \alpha \geq \beta. \tag{5}$$

This property is essential for the α-cut propagation method, see Theorem 2.6. In the following example, we introduce the most common fuzzy structures. Namely, the *fuzzy trapezoidal interval* which we will use throughout this work.

Example 2.4. *A particular class of fuzzy sets is the trapezoidal fuzzy set $\tilde{z}$, forming a subset of $\mathcal{F}(Z)$ with $Z \subset \mathbb{R}$. The respective membership function $\mu_{\tilde{z}}$ is described by two upper semi-continuous functions $f_L\colon (-\infty, 0] \to [0,1]$ and $f_R\colon [0,\infty) \to [0,1]$. Here, $f_L(0) = f_R(0) = 1$ with f_L (f_R) is monotonously increasing (decreasing) and $\lim_{z\to-\infty} f_L(z) = 0$ ($\lim_{z\to\infty} f_R(z) = 0$) such that there exist $\ell^*, r^* \in Z$ with $z_\ell^* \le z_r^*$ and*

$$\mu_{\tilde{z}}(z) = \begin{cases} f_L(z^* - z), & z \le z_\ell^*, \\ 1, & z \in (z_\ell^*, z_r^*), \\ f_R(z - z^*), & z \ge r^*, \end{cases} \tag{6}$$

The triangle fuzzy number $\tilde{z} = \langle \ell, z^*, r \rangle$ specified by left and right limit ℓ, r and peak position $z^* = z_\ell^* = z_r^*$ is a special case of the trapezoidal fuzzy set. Figure 2 depicts the propagation of a trapezoidal fuzzy set.

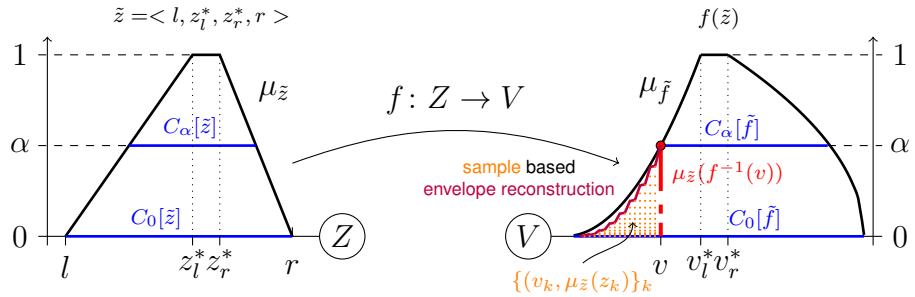

Figure 2: Fuzzy propagation via α-cuts or full sampling and membership reconstruction with $v_k = f(z_k)$, for $Z = V = \mathbb{R}$.

For arbitrary fuzzy sets *Zadeh's extension principle* is the way to propagate uncertainty through a mapping.

Theorem 2.5. *(Zadeh's extension principle [60])*
Consider a function $f\colon Z \to V$ with a non-empty set V. Let $\tilde{z} \in \mathcal{F}(Z)$ with membership function $\mu_{\tilde{z}}$. Define

$$\tilde{f} := f(\tilde{z}) := \{(f(z), \mu_{\tilde{f}}(f(z)) \in V \times [0,1], z \in Z\} \tag{7}$$

with membership function $\mu_{\tilde{f}}$ defined as

$$\mu_{\tilde{f}}(v) := \begin{cases} \sup\limits_{z \in f^{-1}(v)} \mu_{\tilde{z}}(z) & f^{-1}(v) \neq \emptyset, \\ 0 & f^{-1}(v) = \emptyset, \end{cases} \quad \text{for all } v \in V. \tag{8}$$

Then $\tilde{f} \in \mathcal{F}(V)$ with membership function $\mu_{\tilde{f}}$.

If more underlying structure is given, the extension principle can be formulated equivalently in terms of constrained optimization. Zadeh's principle can be reformulated into the so-called α-cut propagation for fuzzy vectors and fuzzy domains to reduce the computational costs.

Theorem 2.6. *(α-cut propagation [40])*
Let $f\colon Z \to V$ be continuous between metric spaces (Z, d_1) and (V, d_2) and let $\tilde{z} \in \mathcal{F}(Z)$ with support $C_0[\tilde{z}] \subset K \subset Z$ for a compact set K with convex Z. Furthermore, let the membership

function $\mu_{\tilde{z}}$ be quasi-concave and upper semi-continuous. Then $\mu_{\tilde{f}}$ can be characterised via α-cuts as

$$C_\alpha[\tilde{f}] = f(C_\alpha[\tilde{z}]). \tag{9}$$

Moreover, if $V = \mathbb{R}$ then

$$C_\alpha[\tilde{f}] = \left[\min_{z \in C_\alpha[\tilde{z}]} f(z), \max_{z \in C_\alpha[\tilde{z}]} f(z) \right]. \tag{10}$$

Note that (9) follows from the assumption that $C_\alpha[\tilde{z}]$ is closed and consequently compact as it is a closed subset of a compact set K in a metric space. Since f is assumed to be continuous, compact sets are mapped to compact sets.

Comparing Zadeh's principle with the α-cut propagation, we immediately see that the former requires the inverse image and an optimization step for each point v whereas the later only depends on two optimization steps of f for the number of α-cuts. Since it is infeasible to perform Zadeh's principle for all points $v \in V$, it is combined or replaced with a sampling approach. We distinguish two variants to sample in V:

- *Semi sampling approach*: directly solve the constrained optimization problem with a global optimiser. For a given sequence $(v_k)_k \subset V$, compute the supremum over $Z_k := \{z \in Z : f(z) = v_k\}$, see the red line in Figure 2.
- *Full sampling approach*: choose a sequence $(z_k)_k \subset Z$, compute $(f_k)_k = [f(z_k)]_k$ and $(\mu_k)_k = [\mu_{\tilde{z}}(z_k)]_k$. Use the data sample pairs (v_k, μ_k) and reconstruct $\mu_{\tilde{f}}$, *e.g.* by convex hull or an envelope approach, see the orange/purple graphics in Figure 2.

For a reliable sample propagation, sufficiently many samples in critical regions are required. Such a region may for instance represent configurations that effect an extreme but possible behaviour of a system, which is unknown a-priori. If such a critical region is missed, the behaviour of the system is misrepresented and the propagation fails.

The α-cut propagation — if applicable — is more reliable than both sampling approaches. If the optimization is performed correctly, it is impossible that a critical sample is missed. In this case, the optimiser has the task to find the critical regions. Formally, the approach reads

- *α-cut propagation*: Based on (10) in Theorem 2.6 with $V = \mathbb{R}$ for a given discretisation $\alpha \in \{\alpha_1, \dots, \alpha_l\} \subset [0, 1]$, compute $C_\alpha[\tilde{f}]$ and build $\mu_{\tilde{f}}$ based on interpolation between the obtained points, see the blue lines in Figure 2.

If f has high evaluation costs, the propagation inevitably becomes difficult and costly. This for example is the case if f represents a finite element solution with a large number of elements. Thus, a surrogate model $f_h \approx f$ is needed to still render the propagation feasible. The main requirement for such a surrogate model is to represent the model accurately in the critical regions. In the numerical experiments, such critical regions are highlighted and the accuracy of the used surrogates is verified.

2.2 Upscaling of heterogeneous linear elastic material

In the following we develop a numerical homogenisation method which yields a macroscopic material based on microscopic properties. The goal of the approach is to dispose of the computationally

involved microstructure and construct an upscaled material surrogate with similar homogenised behaviour on a larger scale. Equivalent terms for "homogenised behaviour" are macroscopic, effective or upscaled behaviour [9], where the examined "behaviour" is subject to some quantity of interest (e.g. average displacement or stress) based on the system response.

In classical (asymptotic) homogenisation, an effective property is calculated based on the assumption of an infinite periodic domain [51]. The local microscopic structure is defined in terms of a representative volume element, which in our setting would consist of a single inclusion that has identical shape in the entire domain. For problems in non-periodic media, the methods of numerical homogenisation or numerical upscaling as e.g. described in [39] are used, where local boundary value problems are solved to calculate effective characteristics in each local domain [44], also see [1, 31, 22] for analytical stochastic homogenisation. Periodic boundary conditions (PBCs) are commonly used for numerical upscaling methods of matrix composite material [13, 46]. In this work, we focus on numerical homogenisation with PBCs for linear elasticity. Let $D = [-1,1]^2$ be a unit cell domain and let the heterogeneous material law be encoded in a tensor $\boldsymbol{C} = \boldsymbol{C}(x) \in \mathbb{R}^{2,2,2,2}, x \in D$. For given macroscopic strain $\boldsymbol{E}$ write the displacement $\boldsymbol{u}$ as $\boldsymbol{u}(x) = \boldsymbol{E} \cdot x + \boldsymbol{v}$ where the D-periodic fluctuation $\boldsymbol{v}$ solves

$$\left\{ \begin{array}{rcll} \operatorname{div} \boldsymbol{\sigma} & = & 0 & \text{in } D, \\ \boldsymbol{\sigma} & = & \boldsymbol{C} \colon \boldsymbol{\epsilon} & \text{in } D, \\ \boldsymbol{\epsilon} & = & \boldsymbol{E} + [\nabla \boldsymbol{v} + \nabla^T \boldsymbol{v}]/2 & \text{in } D, \end{array} \right. \tag{11}$$

such that $\boldsymbol{\sigma} \cdot \mathbf{n}$ is antiperiodic on D with $\boldsymbol{n}$ denoting the outer normal with respect to ∂D. Let $\langle \boldsymbol{\epsilon} \rangle$ and $\langle \boldsymbol{\sigma} \rangle$ denote the average strain and stress of the computed strain $\boldsymbol{\epsilon}$ and stress $\boldsymbol{\sigma}$. Then there exists a tensor $\mathcal{H} \in \mathbb{R}^{2,2,2,2}$ satisfying

$$\langle \boldsymbol{\epsilon} \rangle = \mathcal{H} : \langle \boldsymbol{\sigma} \rangle. \tag{12}$$

The tensor $\mathcal{H}$ is called the effective or upscaled (macroscopic) tensor, representing the elastic moduli of the homogenised medium. By construction it holds that $\boldsymbol{E} = \langle \boldsymbol{\epsilon} \rangle$. Consequently, $\mathcal{H}$ can be obtained from (12) by choosing macro strains $\boldsymbol{E}$ corresponding to different elementary load cases and subsequently computing $\langle \boldsymbol{\sigma} \rangle$ by solving (11). In what follows, the homogenisation technique will be applied for every shape parametrisation encoded in $\boldsymbol{C}$.

2.3 Measuring the distance between constitutive tensors

Constitutive tensors $\boldsymbol{C} = (C_{ijkl}) \in \mathbb{R}^{d,d,d,d}$ in the planar case of $d = 2$ determine the behaviour of the linear elastic material by relating stress and strain. Such a tensor is said to be in $\mathbb{E}\mathrm{la}(d)$ if the symmetry property

$$C_{ijkl} = C_{jikl} = C_{ijlk} = C_{klij}$$

holds. A tensor $\boldsymbol{C} \in \mathbb{E}\mathrm{la}(d)$ may exhibit further symmetry properties. If there exists Lamé constants $\lambda, \mu \in \mathbb{R}$ such that

$$\boldsymbol{C}_{\mathrm{iso}} = \lambda \mathbf{1} \otimes \mathbf{1} + 2\mu \mathbf{I}, \quad I_{ijk\ell} = \frac{1}{2} \left(\delta_{ik}\delta_{j\ell} + \delta_{i\ell}\delta_{jk} \right), \quad \mathbf{1}_{ij} = \delta_{ij},$$

the tensor is called *isotropic*. For orthotropic tensors, we define a rotation matrix

$$g(\theta) = \begin{pmatrix} \cos(\theta) & -\sin(\theta) \\ \sin(\theta) & \cos(\theta) \end{pmatrix}, \quad \theta \in [0, 2\pi]$$

and the *full orthogonal* group operation $o(g)$ via

$$(o(g)\mathbf{C})_{ijk\ell} = g_{ip}g_{jq}g_{kr}g_{\ell s}C_{pqrs}, \quad \boldsymbol{C} \in \mathbb{E}\mathrm{la}(d).$$

We then say that $\boldsymbol{C}_{\text{ortho}} \in \mathbb{E}\mathrm{la}(d)$ is *orthotropic* if it can be represented as

$$\boldsymbol{C}_{\text{ortho}} = \boldsymbol{C}_{\text{iso}} + T, \quad T = \rho(g(\theta))\left(\Lambda_1\mathbf{E}^1 + \Lambda_2\mathbf{E}^2\right), \tag{13}$$

for some isotropic $\boldsymbol{C}_{\text{iso}} \in \mathbb{E}\mathrm{la}(d)$, $\Lambda_1, \Lambda_2 \in \mathbb{R}$, $\theta \in [0, 2\pi]$ and tensors $\boldsymbol{E}^1$ and $\boldsymbol{E}^2$ given in Kelvin-Mandel matrix representation [33] as

$$\frac{1}{\sqrt{2}}\begin{bmatrix} 1/2 & -1/2 & 0 \\ -1/2 & 1/2 & 0 \\ 0 & 0 & -1 \end{bmatrix} \quad \text{and} \quad \frac{1}{\sqrt{2}}\begin{bmatrix} 1 & 0 & 0 \\ 0 & -1 & 0 \\ 0 & 0 & 0 \end{bmatrix}.$$

Note that any isotropic $\boldsymbol{C}_{\text{iso}} \in \mathbb{E}\mathrm{la}(d)$ is invariant under action of $\rho(g)$, in particular $\rho(g)\boldsymbol{C}_{\text{iso}} = \boldsymbol{C}_{\text{iso}}$. With that representation, any orthotropic tensor has 5 degrees of freedom $(\lambda, \mu, \Lambda_1, \Lambda_2, \theta)$. The orthotropic tensors represented in *normal form* have only 4 degrees of freedom since θ is chosen as zero. Let $\mathbb{E}\mathrm{la}(d, \text{iso}), \mathbb{E}\mathrm{la}(d, \text{ortho}) \subset \mathbb{E}\mathrm{la}(d)$ be the set of all isotropic and orthotropic tensors, respectively. Given any anisotropic tensor $\boldsymbol{C}$, we define the distance to the symmetry class of isotropic and orthotropic tensors by

$$d_{\text{iso}}(\boldsymbol{C}) = \min_{\boldsymbol{X}\in\mathbb{E}\mathrm{la}(d,\text{iso})} \|\boldsymbol{C} - \boldsymbol{X}\|, \quad d_{\text{ortho}}(\boldsymbol{C}) = \min_{\boldsymbol{X}\in\mathbb{E}\mathrm{la}(d,\text{ortho})} \|\boldsymbol{C} - \boldsymbol{X}\| \tag{14}$$

with the Frobenius norm $\|\cdot\|$. The distances to the symmetry classes can be characterised as follows.

Proposition 2.7. *(**Distance to isotropy class** [2])*
Let $\boldsymbol{C} \in \mathbb{E}\mathrm{la}(d)$ for $d = 2$. Define $\boldsymbol{C}_{iso} = 2\mu\boldsymbol{I} + \lambda\mathbf{1}\otimes\mathbf{1}$ with

$$\lambda := \frac{1}{8}(C_{1111} + 6C_{1122} - 4C_{1212} + C_{2222})$$
$$\mu := \frac{1}{8}(C_{1111} - 2C_{1122} + 4C_{1212} + C_{2222})$$

as the orthogonal projection of $\boldsymbol{C}$ onto the isotropic material class. Then,

$$d_{iso}(\boldsymbol{C}) = \|\boldsymbol{C} - \boldsymbol{C}_{iso}\|. \tag{15}$$

Proposition 2.8. *(**Distance to orthotropy class** [2])*
Let $\boldsymbol{C} \in \mathbb{E}\mathrm{la}(d)$ for $d = 2$ and $(\theta_k)_{k=1}^K$, $K \in \mathbb{N}$ be the finite roots of

$$a\cos 8\theta + b\sin 8\theta + c\cos 4\theta + d\sin 4\theta = 0, \quad \theta \in [0, 2\pi]$$

with $a = 4X_1Y_1$, $b = 2(Y_1^2 - X_1^2)$, $c = 2X_2Y_2$ and $d = Y_2^2 - X_2^2$ and

$$X_1 = \frac{1}{2\sqrt{2}}(C_{1111} - 2C_{1122} - 4C_{1212} + C_{2222}),$$
$$Y_1 = \sqrt{2}(C_{1112} - C_{2212}),$$
$$X_2 = \frac{1}{\sqrt{2}}(C_{1111} - C_{2222}),$$
$$Y_2 = \sqrt{2}(C_{1112} + C_{2212}.$$

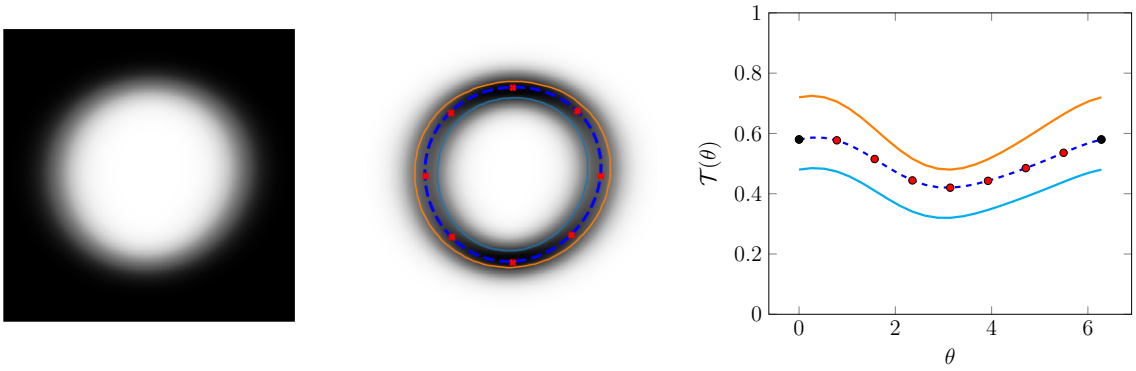

Figure 3: **Left**: Example of a blurred image of an inclusion in a composite material. **Center**: the same image after the application of a gradient filter with sketch of the relation between sample points. **Right**: The radial trigonometric function $\mathcal{T}(\theta, R)$, $R \in \mathbb{R}^8$.

For $\theta \in [0, 2\pi]$, *define*

$$\Lambda_1(\theta) := X_1 \cos 4\theta + Y_1 \sin 4\theta, \quad \Lambda_2(\theta) := X_2 \cos 2\theta + Y_2 \sin 2\theta$$

and

$$\boldsymbol{X}(\theta_k) := \rho(g(\theta_k))(\Lambda_1(\theta_k)\boldsymbol{E}^1 + \Lambda_2(\theta_k)\boldsymbol{E}^2) \quad \textit{for} \quad k = 1, \dots, K.$$

Then,

$$d_{\textit{ortho}}(\boldsymbol{C}) = \min_{k=1,\dots,K} \|\boldsymbol{C} - \boldsymbol{X}(\theta_k)\|. \tag{16}$$

With the introduced material class concepts of constitutive tensors we are able to measure the distance of our effective material to the isotropic respectively orthotropic material class for each shape parametrisation.

3 Fuzzy Edge Detection

Given a blurred image as depicted in Figure 3, the most common approach to reconstruct the original image is to use some method from the wide class of *blind deconvolution* methods [28]. These methods assume that an image y is the convolution of an original image x and some kernel k, distorted with additive noise n, i.e.,

$$y = x \star k + n.$$

Finding a pair (x, k) satisfying this equation is equivalent to de-blurring the image, leading to *a* original image x. This however is an ill-posed problem, since an infinite number of such pairs can be found [54], making some form of regularisation inevitable. The classical approaches assume zero noise and employ regularised least squared methods [11, 26, 35]. Each regularisation is based on assumptions of the kernel and the original image. More recently, natural image statistics and the Bayesian framework were used to formulate such assumptions more precisely and thus improved the performance of blind deconvolution methods, see [30, 32, 50] for a first overview. Simply put, prior knowledge and the ability to incorporate this knowledge improve the deconvolution result. However, we are in a different situation

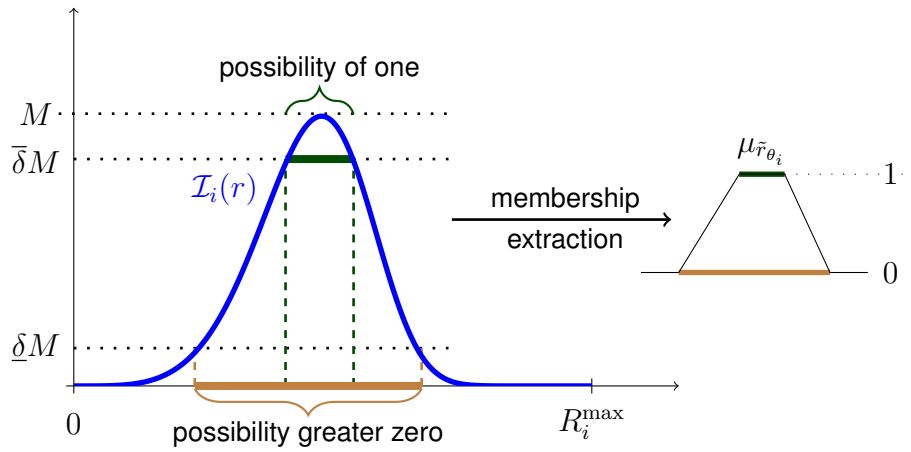

Figure 4: Construction of a trapezoidal membership function $\mu_{\tilde{r}_{\theta_i}}$ as in (6) obtained from a intensity function $\mathcal{I}_i$ for given angle θ_i and thresholds $0 < \underline{\delta} < \overline{\delta} < 1$.

since we miss this prior knowledge and we are shall not be inclined to make unverifiable assumptions. Furthermore, we are not primarily interested in the most probable reconstructed image x. Instead, we want a set of possible boundaries given a blurred image and a small set of assumptions. Therefore, we introduce the *fuzzy edge detection* which is based on three simple assumptions

(a) Each inclusion is a *star-shaped*, i.e. there exist a midpoint from which each boundary point is reached by a straight line.

(b) The gradient of the blurred image yields a connected domain and the boundary of the inclusion lies in this connected domain.

(c) Each boundary curve has a limited prescribed variation.

These three assumptions implicitly define a possible set of boundary curves provided a blurred image. Any of these boundary curves is possible but nothing can be said about the probability of each curve. Since we assume a star-shaped inclusion, a radial function $r(\theta) : [0, 2\pi) \mapsto \mathbb{R}_+$ is able to describe the boundary of this inclusion. The uncertainty of the boundary is then captured in a fuzzy function $\tilde{r}$.

In order to construct a fuzzy function $\tilde{r}$ from a blurred image $D = [-1, 1]^2$, we use trigonometric interpolation on a vector of $N \in \mathbb{N}$ fuzzy numbers. Each component of the fuzzy vector denoted by

$$\tilde{R}_N := \tilde{R}_N[\Theta] := (\tilde{r}_{\theta_1} \ \cdots \ \tilde{r}_{\theta_N}) \tag{17}$$

is constructed from a radial cut (i.e. a line segment) that starts in the center and ends at the outer boundary for a prescribed set of angles $\Theta = \left\{\theta_i = \frac{2\pi i}{N+1} \mid i = 1, \dots, N\right\}$. The continuous function $\mathcal{I}_i : [0, R_i^{\max}] \to \mathbb{R}_+$ with $R_i^{\max} = 1/\max\{|\cos\theta_i|, |\sin\theta_i|\}$ determines the intensity of the gradient along this radial cut, see Figure 4 for an illustration. The information encoded in $\mathcal{I}_i$ is used to construct a trapezoidal fuzzy number. For this, consider lower and upper percentage threshold values $0 < \underline{\delta} < \overline{\delta} < 1$ and determine $M := \max_{r\in[0,R_i^{\max}]} \mathcal{I}_i(r)$. If the intensity in one point is larger than $\overline{\delta}M$, it is assigned a possibility of one. If it is smaller than $\underline{\delta}M$, it gets assigned a possibility of zero. For simplicity, in between these thresholds we assign a possibility by linear interpolation. This algorithm yields a membership function $\mu_{\tilde{r}_{\theta_i}}$ of trapezoidal form, which is illustrated in Figure 4.

Gathering these fuzzy numbers into a vector yields the non-interactive fuzzy vector $\tilde{R}_N$, encoded in the membership function

$$\mu_{\tilde{R}_N} = \min\{\mu_{\tilde{r}_{\theta_1}}(r_1), \dots, \mu_{\tilde{r}_{\theta_N}}(r_N)\},$$

where non-interactivity means that the value of one sample does not influence the membership function of another value. Let $R = (r_1 \ \cdots \ r_N) \in C_0[\tilde{R}_N]$ and denote the trigonometric interpolation by $\mathcal{T}(\cdot, R)$. It represents the mapping from interpolation points onto the trigonometric polynomials. This mapping is bijective if the degree of freedom coincides with the number of interpolation points. The coefficients are efficiently computed via a discrete Fourier transformation and the interpolation scheme yields convergence rates as follows.

Proposition 3.1. ***(Trigonometric interpolation)***
Let $f \in \mathcal{C}^k_{\mathrm{per}}(0, 2\pi)$ describe the boundary of a star shaped inclusion in $\mathbb{R}^2$, then there exists $c = c(k, f, f^{(k)}) > 0$ such that

$$\|f - \mathcal{T}(\cdot; [f(\theta_1), \ldots, f(\theta_N)])\|_{L^2(0,2\pi)} \leq cN^{-k}.$$

Given all possible interpolation points $R \in C_0[\tilde{R}_N]$, we define the a set of radial boundary functions describing the interface as

$$B_N = \left\{ \mathcal{T}(\cdot; R) \mid R \in C_0[\tilde{R}_N] \right\}.$$

Note that $\mathcal{T}(\cdot; \tilde{R}_N)$ defines a fuzzy function [38]. The number of cuts and thus the number of interpolation points N is setted according to the accuracy required by the considered problem. With sufficiently many interpolation points, the set B_N can represent highly oscillatory boundaries, see Figure 8 for $N = 16$. For the sake of efficiency, the interpolation should be carried out with as few points as possible, which demands an adequate knowledge about the properties (in particular smoothness/roughness) of the physical system at hand. We choose the total variation of the radial function as a measure for roughness, which is defined for $R \in C_0[\tilde{R}_N]$ as

$$\mathrm{TV}(R) = \int_0^{2\pi} |\mathcal{T}'(\theta; R)| \ \mathrm{d}\theta.$$

Given some bound $0 \leq b \leq \infty$, the TV restricted set of radial boundary function based on N grid points is defined by

$$B_{N,b} := \left\{ \mathcal{T}(\cdot; R) \colon [0, 2\pi] \to \mathbb{R}_+ \mid R \in C_0[\tilde{R}_N] \text{ and } TV(R) \leq b \right\}. \tag{18}$$

With this construction, we may define the interactive fuzzy set

$$\tilde{R}_{N,b} := \left\{ (R, \mu_{\tilde{R}_{N,b}}) | \, R \in C_0[\tilde{R}_N] \text{ and } \mathrm{TV}(R) \leq b \right\}, \tag{19}$$

$$\mu_{\tilde{R}_{N,b}} := \mu_{\tilde{R}_N} \mathbf{1}_{\{R | TV(R) \leq b\}}, \tag{20}$$

where $\mathbf{1}_X$ denotes the characteristic function on a set X. In Section 3.1 we make clear that the fuzzy set in (19) in fact defines a fuzzy vector. This in turn motivates the α-cut propagation of fuzzy uncertainty, introduced in Section 2.1. In particular, consider a continuous real valued function $\mathcal{Q}$ defined on the compact set $C_0[\tilde{R}_N]$, which is the 0-cut of the non-interactive fuzzy vector $\tilde{R}_N$ from (17). The propagated uncertainty of the interactive fuzzy set $\tilde{R}_{N,b}$ through $\mathcal{Q}$ is then captured on each α-level

$$C_\alpha[\tilde{\mathcal{Q}}_b] := \left[\min_{R \in C_\alpha[\tilde{R}_{N,b}]} \mathcal{Q}(R), \max_{R \in C_\alpha[\tilde{R}_{N,b}]} \mathcal{Q}(R) \right] \tag{21}$$

of the fuzzy set $\tilde{\mathcal{Q}}_b := \mathcal{Q}(\tilde{R}_{N,b})$. We emphasise that $C_0[\tilde{R}_N]$ defines a tensor domain on which $\mathcal{Q}$ is well defined, *i.e.*

$$C_0[\tilde{R}_N] = \bigtimes_{i=1}^{N} C_0[\tilde{r}_{\theta_i}], \tag{22}$$

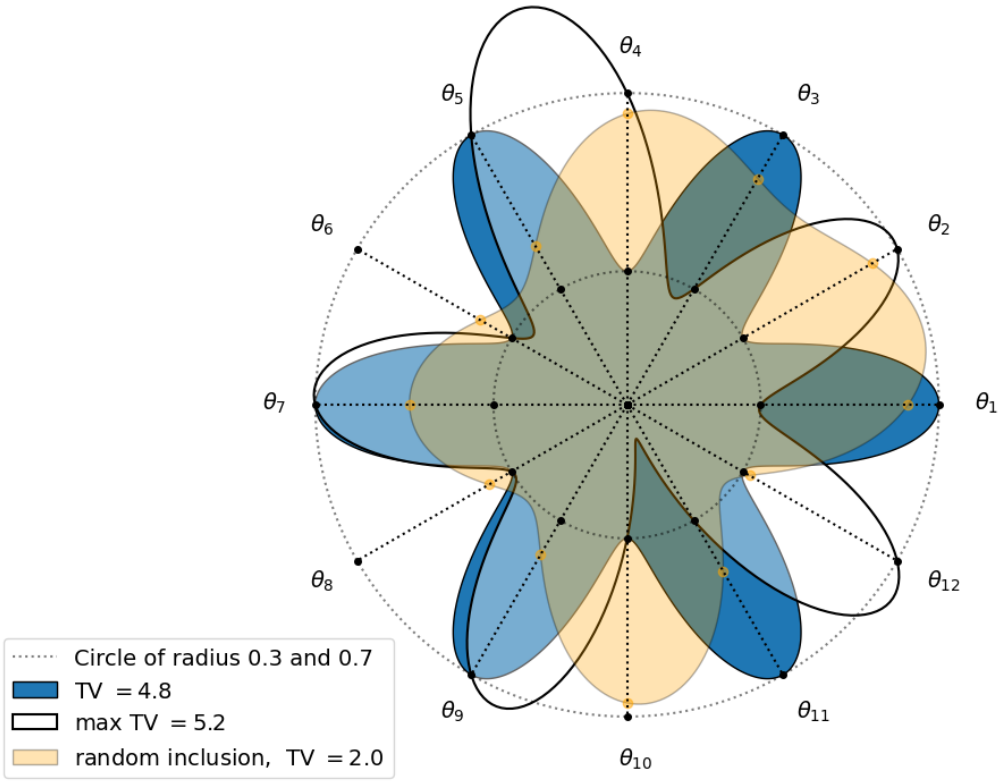

Figure 5: Influence of the total variation with underlying trigonometric interpolation for $N = 12$ and $R \in C_0[\tilde{R}_N] = [0.3, 0.7]^N$.

a fact that becomes useful when applying low-rank tensor formats in the upcoming Section 4.2 as surrogate models for $\mathcal{Q}$. However, the computation of $\tilde{Q}_b$ only requires evaluation of $\mathcal{Q}$ on $C_0[\tilde{R}_{N,b}] \subset C_0[\tilde{R}_N]$, which in general is not a tensor domain.

3.1 Properties of the TV bounded fuzzy set $\tilde{R}_{N,b}$

The total variation determines the shape of the inclusion. With a very small total variation, the shapes become more and more circular. Any circular shape, independent of the radius, has a total variation of zero. We want to point out, that we do not measure the total variation of the trajectory, where the total variation of a circle would be larger than zero. Instead we measure the total variation of the radial function.

In Figure 5 shapes with different total variations are depicted. The blue shape is generated by taking alternating radii, the white shape is the result of optimization. The maximal total variation is 5.2 for $N = 12$, whereas a randomly generated shape has a total variation of around 2. With increasing N the maximal total variation would also increase.

Note that the resulting shapes may *violate* the boundaries in between the sampling points. Especially, the maximum total variation solution. This can be resolved with more sampling points, a sufficiently strict tv bound or by replacing the trigonometrical interpolation with a corresponding spline interpolation.

Bounding the total variation leads to interaction of the fuzzy set $\tilde{R}_{N,b}$. Figure 6 illustrates the interaction

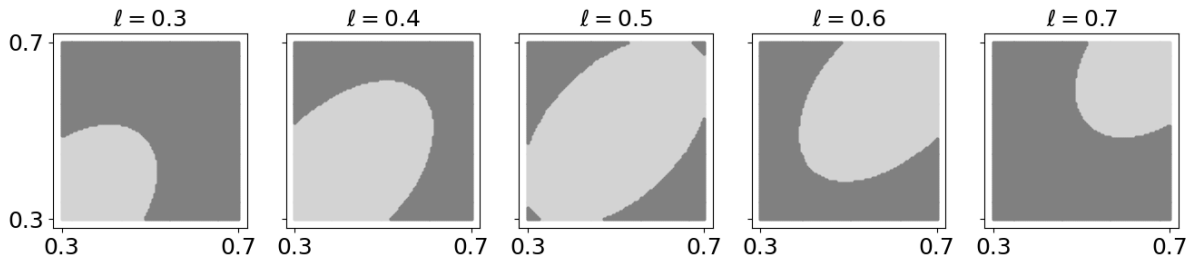

Figure 6: Slices of the constrained support of $\tilde{R}_{N,b}$ in light gray based on $C_0[\tilde{R}_N] = [0.3, 0.7]^N$ with $N = 3$ and $b = 1$. From left to right: $C_0[\tilde{R}_{N,b}] \cap [0.3, 0.7]^2 \times \{\ell\}$ with $\ell = 0.3, 0.4, 0.5, 0.6, 0.7$.

for the case $N = 3$. It shows that fixing one point constraints the remaining points to the light gray area. Hence the possibility outside this area is zero. In a non-interactive setting the possibility could be strictly larger than zero. Consequently, the total variation bound restricts the set of possible curves. The Figure indicates that the set of valid radial points is convex, which is shown in the following proposition.

Proposition 3.2. *(**Convexity of TV constrained domain**)*
Let $N \in \mathbb{N}$. Then for $b \geq 0$ the 0-cut $C_0[\tilde{R}_{N,b}]$ defines a convex set.

Proof. Let $R_1, R_2 \in \operatorname{supp} \tilde{R}_N$, $t \in [0, 1]$ and define $R_t = tR_1 + (1 - t)R_2$. The radial function to describe the boundary then takes the form

$$\mathcal{T}(\phi, R_t) = \sum_{k=0}^{N-1} a_k[R_t] e^{ik\phi}$$

with imaginary number i and coefficients $a_i[R_t]$. Since the Fourier interpolation defines a linear operator, it holds $a_i[R_t] = ta_i[R_1] + (1 - t)a_i[R_2]$. Thus, by triangle inequality it follows that

$$TV(R_t) \leq tTV(R_1) + (1 - t)TV(R_2) \leq b.$$

□

Consequently the α-cuts of $\tilde{R}_{N,b}$ are nested and convex.

Proposition 3.3. *(**Characterisation of** $\tilde{R}_{N,b}$)*
Let $b \geq 0$ and $\tilde{R}_N$ be a fuzzy (domain) vector with $C_1[\tilde{R}_N] \subset C_0[\tilde{R}_{N,b}]$. Then $\tilde{R}_{N,b}$ defines a fuzzy (domain) vector.

Note that for given N, there always exists $b = b(N)$ such that the conditions of Proposition 3.3 hold true. In particular, for b large enough it holds $\tilde{R}_N = \tilde{R}_{N,b}$. Consequently, the α-cut propagation (21) can be applied.

4 Accelerated emulation of fuzzy effective material

The fuzzy edge detection described above yields a fuzzy set $R \in \mathbb{R}^N$. Trigonometric interpolation then results in a boundary representation of the inclusion. In the following, we define a composite material based on this representation.

Consider the square $[-1,1]^2$ on which we define a two phase composite material $\boldsymbol{C}(x) = \boldsymbol{C}(x,R)$ with $\boldsymbol{C}_{\text{incl}}, \boldsymbol{C}_{\text{matrix}} \in \mathbb{E}\text{la}(d, \text{iso})$. This description represents a piecewise isotropic material with star-shaped inclusion defined as

$$\boldsymbol{C}(x,R) := \begin{cases} \boldsymbol{C}_{\text{incl}}, & r \leq \mathcal{T}(\theta,R), \\ \boldsymbol{C}_{\text{matrix}}, & \text{else}, \end{cases} \qquad x = r[\cos(\theta), \sin(\theta)], \tag{23}$$

such that $0 < R_{\text{min}} < \mathcal{T}(\theta,R) < R_{\text{max}} < 1$ uniform in θ and R.

Given a fixed R, the homogenisation from Section 2.2 yields the constitutive tensor $\boldsymbol{C}(\cdot,R) \in \mathbb{E}\text{la}(d)$ for the upscaled macroscopic material. In Voigt notation, this mapping is denoted as

$$R \mapsto \mathcal{H}(R) = \begin{bmatrix} H_{11} & H_{12} & H_{13} \\ & H_{22} & H_{23} \\ \textit{sym} & & H_{33} \end{bmatrix} (R) \in \mathbb{R}^{3,3}, \tag{24}$$

with symmetric positive definite matrix $\mathcal{H}(R) \in \mathbb{R}^{3,3}$. It in general describes an anisotropic material since the involved geometry of the inclusion may lack any type of symmetry.

We would like to point out that the parametric dependency $R \to \boldsymbol{C}(\cdot,R)$ does not define a continuous function with images in $L^\infty(D)^{d,d,d,d}$ since marginal changes of the shape of the inclusion immediately yield an L^∞ error equal to the contrast $\|\boldsymbol{C}_{\text{incl}} - \boldsymbol{C}_{\text{matrix}}\|_F$ with Frobenius norm $\|\cdot\|_F$. Despite this discontinuity and its effect on the regularity of the parametric solution $R \to \boldsymbol{u}(R)$, the parametric homogenised tensor (24) defines a continuous map.

Recall that the evaluation of $\mathcal{H}$ involves multiple simulations of periodic linear elastic boundary value problems of the form (11). To accelerate the upscaling process, in the following we replace the *simulator* with an *emulator*. The emulator relies on a mesh discretisation of the domain D and a group of tensor train surrogates to approximate $\mathcal{H}$, which is discussed in Section 4.2.

If D is discretised by an automatic mesh generator under the constrained of equal amount of vertices on the inclusion's boundary and on the boundary of D for any R, the resulting mesh map $R \mapsto \mathcal{M}(R)$ in general is discontinuous. As a consequence, a mesh dependent finite element computation may inherit the lack of continuity even through the whole geometry has smooth dependence on R, see Figure 7 for an example. This in turn aggravates optimization based on gradient information. We solve this issue in Section 4.1 by constructing a family of transformed meshes with smooth dependence on R.

4.1 Constructive smooth transformation of meshes

For $n \in \mathbb{N}$ interpolation points, consider the composite interface discretisation

$$\mathcal{T}_n(R) := \{x = \mathcal{T}(\theta_i,R)[\cos(\theta_i)\ \sin(\theta_i)]^\top, \theta_i = 2\pi i/n, i = 0,\dots,n-1\}.$$

We now construct a smooth diffeomorphism that creates meshes based on a single reference mesh $\hat{\mathcal{M}}$ denoted as $\Psi\colon \mathbb{R}^d \times \mathbb{R}^N \to \mathbb{R}^d$ such that $\Psi(\hat{\mathcal{M}},R) = \mathcal{M}(R)$. Let $R_{\text{ref}} = [0.5,\dots,0.5] \in \mathbb{R}^N$ and $\mathcal{T}(\cdot,R_{\text{ref}})$ define a circular inclusion with radius 0.5. Consider a fixed reference mesh discretisation $\mathcal{M}_{\text{ref}}$ of $[-1,1]^2$ such that

- there is a fixed number of nodes on the boundary $\partial[-1,1]^2$

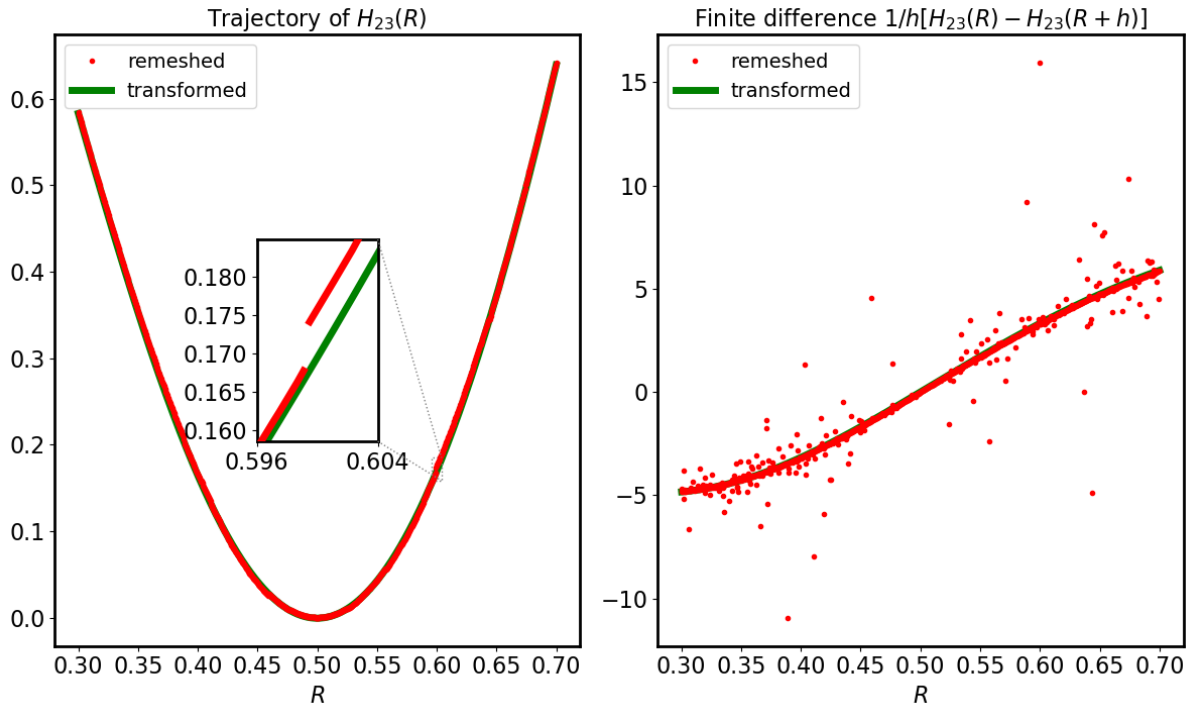

Figure 7: Illustration of discontinuity of the homogenisation map $R \to \mathcal{H}(R)$ from (24) for $N = 3$ corresponding to fixing two radial sample points to 0.5, while running through the last sample point from 0.3 to 0.7. The red lines are based on computations using automatic mesh generation with a fixed number of mesh vertices on ∂D and on the circle interface. The green lines are computed with meshes constructed with the diffeomorphism Ψ from (25). **Left**: Trajectory of H_{23}. On the macroscale, both curves seem to coincide. The discontinuity becomes visible when zooming in. **Right**: Finite difference plot of H_{23}. The red markers demonstrates the extent of discontinuity of H_{23}, while the green line remains smooth.

- any node in $\mathcal{F}_n(R_{\text{ref}})$ is part of the mesh.

Compute the sets $\mathcal{F}_{2n}(R_{\text{ref}})$ and $\mathcal{F}_{2n}(R)$ corresponding to higher discrete resolution of the reference or target interface. The transformation Ψ then consists of two parts as follows. First, let $\{\phi_i\}$ form a smooth partition of unity of $[0, 2\pi]$ with $\phi_i(i\pi/n) = 1$ and $\operatorname{supp}\phi_i = [(i-1)\pi/n, (i+1)\pi/n]$. This function set deals with the angular part of the transformation. Second, let $\chi_i \in \mathcal{C}^k[0, \sqrt{2}]$ be a set of splines with $k \geq 2$ for the radial part of the transformation with the following properties:

1 The reference radius is mapped onto the transformed radius, i.e.

$$\chi_i(\mathcal{T}(\theta_i, R_{\text{ref}})) = \mathcal{T}(\theta_i, R).$$

2 The spline is strong monotonically increasing on $(R_{\text{min}}, R_{\text{max}})$ and otherwise equals the identity map.

Altogether, the transformation reads

$$\Psi(\hat{x}, R) := \sum_{i=1}^{2n} \chi_i(\hat{r})\phi_i(\hat{\theta}), \quad \hat{x} = \hat{r}[\cos\hat{\theta}, \sin\hat{\theta}]^\top. \tag{25}$$

We refer to Figure 8 for an illustration of the capacity of the constructed map Ψ, which is characterised next.

Proposition 4.1. *($\mathcal{C}^k$ **diffeomorphism**)*
The map $\Psi : [-1, 1]^2 \to [-1, 1]^2$ is bijective and k-times continuously differentiable.

Proof. The bijectivity follows from strong monotonicity in radial direction and the smooth partition of unity in angular direction. The smoothness of ϕ_i and of the polar coordinate mapping away from zero is given since χ_i is k-times continuous differentiable. For $i = 1, \dots, 2n$ the desired property follows immediately. □

4.2 Tensor trains based emulation

Assume some function $f\colon C_0[\tilde{R}] \subset \mathbb{R}^N \to \mathbb{R}$ with $C_0[\tilde{R}] = \bigtimes_{i=1}^N C_0[\tilde{R}_i]$. For $f = H_{ij}$, $1 \leq i \leq j \leq 3$ we consider surrogates of the form

$$f(R) \approx f_\Lambda(R) := \sum_{\alpha\in\Lambda} \boldsymbol{U}[\alpha]\Pi_\alpha(R), \quad \Lambda = \bigtimes_{i=1}^N \Lambda_i \subset \mathbb{N}^N,\ |\Lambda| < \infty, \tag{26}$$

based on a polynomial feature class $\Pi := \{\Pi_\alpha, \alpha \in \mathbb{N}^N\}$ where each polynomial $P_\alpha \in \Pi$ is of tensorised form $\Pi_\alpha = \bigotimes_{i=1}^N q^i_{\alpha_i}$ with one dimensional polynomials $\{q^i_{\alpha_i}\colon C_0[\tilde{R}_i] \to \mathbb{R}, \alpha_i \in \Lambda_i\}$ for $i = 1, \dots, N$ and unknown coefficient tensor $\boldsymbol{U}\colon \Lambda \to \mathbb{R}$. This model suffers from the curse of dimensionality since the cardinality $|\Lambda|$ grows exponential with respect to the dimension N. A possibility to circumvent this challenge lies in a compressed representation of the coefficient tensor, here based on the *tensor train format* (TT format) [42]. Let $\rho = (\rho_1, \dots, \rho_{N-1}) \in \mathbb{N}^{N-1}$ be the tensor train rank and let $\rho_0 = \rho_N = 1$. We then choose $\boldsymbol{U}$ given in tensor train decomposition by

$$\boldsymbol{U}[\alpha] := U_1[\alpha_1]U_2[\alpha_2]\cdots U_n[\alpha_N], \quad \alpha \in \Lambda, \tag{27}$$

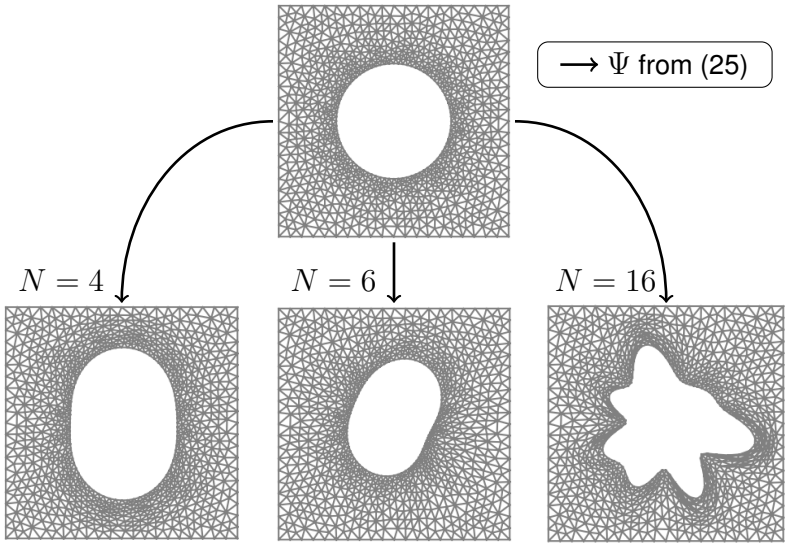

Figure 8: Example of the constructive C^k diffeomorphism Ψ with various target structures parametrised via $R \in \mathbb{R}^N$. Although a mesh is generated inside and outside of the inclusion, the inclusions are illustrated as holes for better visibility. From left to right: Reference mesh and random target meshes with $N = 4, 6, 16$.

with component tensors of order 3, such that $U_i[:] \in \mathbb{R}^{\rho_{i-1},|\Lambda_i|,\rho_i}$ for $i = 1, \dots, N$. The number of degrees of freedom for this design is given as $\sum_{i=1}^{N} \rho_{i-1}|\Lambda_i|\rho_i$, which does not grow exponentially but only linearly in dimension N. Given data $(R^{(k)}, y^{(k)})_{k=1}^{K}$, $K \in \mathbb{N}$ with $y^{(k)} = f(R^{(k)})$, we obtain a surrogate as in (26) by carrying out a regularised empirical regression, namely by solving the optimisation problem

$$\min_{U \text{ as in (27)}} \sum_{k=1}^{K} \|f_\Lambda(R^{(k)}) - y^{(k)}\| + \lambda \|U\|_* \tag{28}$$

with regularisation parameter $\lambda > 0$ and suitable norm $\|\cdot\|_*$. The optimisation problem (28) can be solved by regression with an alternating linear scheme (ALS) [25]. As a modification of the basic ALS, we introduce a scheme for rank adaptivity. This concept offers several advantages to obtain an adjusted tensor train rank which is in general unknown a priori. From a practical point of view, it reduces the computational cost during optimisation while obtaining a prescribed accuracy in the approximation class. Furthermore, starting with a small rank, the iterative process empirically enables the ALS to converge to a solution based on successive computations of initial guesses for models with higher ranks based on the given restricted number of samples. The proposed approach is summarised in Algorithm 1 and the rank adaptivity is presented in Algorithm 2.

A principle of the rank adaptivity is to keep one (control) singular value to monitor the importance of the related rank coupling value during the optimisation process. This additional singular value per rank coupling remains until the end of the regression scheme to prevent oscillation between rank growth and reduction. It ensures an upper bound of the related rank value throughout the entire process. After successful termination of Algorithm 2, the existing (possibly small) control singular value is removed by a final *rounding* [42] of the resulting tensor train. We refer to [25] for more technical details on the basic ALS, *e.g.* with regard to setting and moving the non-orthogonal component (the core) via left and right matricisation and orthogonalisation. Eventually, the overall emulator is obtained by evaluation of the 6 scalar valued tensor train surrogate maps, replacing $R \mapsto [\mathcal{H}(R)]_{ij}$ and $1 \le i \le j \le 3$ corresponding to the upper triangular part of the symmetric matrix $\mathcal{H}(R)$.

Algorithm 1 Rank adaptive empirical tensor train regression via ALS

Require:
$\left(R^{(k)}, y^{(k)}\right)_{k=1}^{K}$ ▷ *training data*,
$\Pi_\alpha, \alpha \in \Lambda$ ▷ *polynomial features*,
$\mathrm{tol}_{\mathrm{MSE}} > 0$ ▷ *desired mean square error (MSE) tolerance*,
$\mathrm{iter}_{\max} \in \mathbb{N}$ ▷ *maximum iteration number*,
$L_{\mathrm{HIST}} \in \mathbb{N}$ ▷ *history length for rank update*,
$\mathrm{tol}_{\mathrm{DECAY}} > 0$ ▷ *minimum decay rate.*

Ensure: Tensor train surrogate f_Λ with rank $\rho \in \mathbb{N}^{N-1}$

```
Set rank ρ to (1, ..., 1)
HIST ← [ ]                                              ▷ MSE history
while MSE > tol_MSE and #HIST < iter_max do
    for i in [1, ..., N, N − 1, ..., 2] do              ▷ forward/backward sweep
        Fix U_j in (27) for j ≠ i.
        Then update U_i by solving (28).
    end for
    Compute MSE and append to HIST.
    DECAY ← Average decay rate of last L_HIST entries in HIST.
    if DECAY < tol_DECAY then
        Apply Algorithm 2 to obtain f_Λ with modified rank ρ*.
    end if
end while
```

Note that non-zero values of H_{13} and H_{23} solely appear when the effective material behaviour is not isotropic or rotational-free orthotropic, *i.e.*, this is described by (13) with $\theta = 0$.

5 Numerical Experiments

This section is concerned with the assessment of the numerical performance of the approach presented above, for which two experiments are examined. In the first experiment, we measure the distance of the upscaled material to the isotropy and orthotropy class. Additionally, we identify configurations that maximise and minimise the respective distances. In the second experiment, we test if the upscaled material is suitable for a worst case analysis, i.e., we test if it is possible to find bounds that envelop the most extreme behaviour of the quantity of interest under consideration. For this, a material with 8×8 arbitrary inclusions placed on a checkerboard is compared to an upscaled material with the same geometrical dimensions. Both experiments demonstrate the efficacy of the fuzzy approach to model uncertainty of the inclusion to identify extremal behaviour and its source.

Three types of computational tasks are performed in the experiments. The foundation is laid by Finite Element (FE) simulations to generate the realisations of constitutive tensors by solving (11). Furthermore, an alternating linear scheme is used to train the surrogate model and for optimization computations to carry out the uncertainty propagation based on α-cuts.

All FE computations are done with the `FEniCS` package [20]. The mesh generation is realised using `Gmsh` [21] and the `Bubbles` package [23]. Moreover, the python package `TensorTrain` [24] is utilised for the rank adaptive tensor train regression and `ALEA` [17] for the underlying polynomial features. The optimization tasks are performed with restarted trust region optimization implemented in `Scipy` [58].

Algorithm 2 Rank adaptivity

Require:
- $U[\alpha] = U_1[\alpha_1] \cdots U_N[\alpha_N]$ ▷ *TT decomposition with rank* $\rho \in \mathbb{N}^{n-1}$
- $\rho_{\max} \in \mathbb{N}^{n-1}$ ▷ *maximal rank limit*
- $\rho_{\mathrm{add}} \in \mathbb{N}$ ▷ *maximal rank increasement*
- $\delta > 0$ ▷ *Dörfler treshold*

Ensure: TT decomposition $U^*[\alpha] = U_1^*[\alpha_1] \cdots U_N^*[\alpha_N]$ with rank ρ^*

Set U_1 as core.
Define operators $\mathcal{L}$ and $\mathcal{R}$ as left and right matricisation of order 3 tensors.
for $k = 1, \ldots, N-1$ **do**
  Perform SVD: $\mathcal{L}(U_k) = V \operatorname{diag}(\sigma) W$, $\sigma \in \mathbb{R}^{r_k}$.
  Define splittings $\sigma^1_{\rho_k^*} = [\sigma_1, \ldots, \sigma_{\rho_k^*}]$ and $\sigma^2_{\rho_k^*} = [\sigma_{\rho_k^*}, \ldots, \sigma_{\rho_k}]$.
  if there exists ρ_k^* with $\delta \|\sigma^1_{\rho_k^*}\|_1 \geq \|\sigma^2_{\rho_k^*}\|_1$ **then** ▷ *possible rank reduction*
    Set $\rho_k^* = \min\{\rho_k, \rho_k^* + 1\}$. ▷ *keep control singular value*
    Set $U_k^* = \mathcal{L}^{-1}(V[:, : \rho_k^*])$.
    Set $U_{k+1} = \operatorname{diag}(\sigma[: \rho_k^*]) W[: \rho_k^*, :]$. ▷ C_{k+1} *becomes next core*
  else ▷ *possible* k*-th rank increase*
    Set $\rho_k^* = \min\{\rho_k + \rho_{\mathrm{add}}, \rho_{\max,k}\}$.
    Set $d = \rho_k^* - \rho_k$
    Extend V with d random columns orthogonal to V.
    Extend σ with d values smaller than $\sigma_{\rho_k^*}$.
    Extend $\mathcal{R}(WU_{k+1})$ with d random rows orthogonal to $\mathcal{R}(WU_{k+1})$.
    Set $U_k^* = \mathcal{R}^{-1}(V)$
    Set $U_{k+1} = \operatorname{diag}(\sigma^*) \mathcal{R}^{-1}(\mathcal{R}(WU_{k+1}))$ ▷ U_{k+1} becomes next core
  end if
end for
Set $U_N^* = U_N$.

The computations are performed with $N = 6$ and $N = 12$ radial sampling points. Here, the $N = 6$ case imposes significantly less computational burden on the surrogate and the optimization than the $N = 12$ case. In particular, our optimization scheme took up to 10^6 evaluations of the $\mathcal{H}(R)$ for $N = 12$ and up to 1×10^5 evaluations for $N = 6$ per propagated quantity of interest. We underline that all optimization tasks involved are non-convex with non-linear cost functions and constraints. Consequently, we take arbitrary points $R \in [0.3, 0.7]^6$ for $N = 6$ and $R \in [0.4, 0.6]^{12}$ — a smaller domain — for $N = 12$. This enables sufficiently non-trivial shapes without rendering the surrogate model and the optimization infeasible. Each realisation R determines a boundary stellar inclusion in terms of a trigonometric interpolation. Inside and outside of the inclusion we assume isotropic material behaviour. Concretely, we let the Young's modulus $E_{\text{incl}} = 3230$ and Poisson ratio of $\nu_{\text{incl}} = 0.3$ in the inside. Outside of the inclusion we choose $E_{\text{matrix}} = E_{\text{incl}}/4$ and $\nu_{\text{matrix}} = 0.2$. These values are transformed into Lamé constants by

$$\lambda = \frac{E\nu}{(1+\nu)(1-2\nu)}, \quad \mu = \frac{E}{2(1+\nu)}.$$

By adaptation to the plane, *adapted* Lamé constants are obtained, namely

$$\lambda^* = \frac{2\lambda\mu}{\lambda + 2\mu}, \quad \mu^* = \mu.$$

Note that the adapted Lamé constants are dimension free.

For a given $R \in C_0[\tilde{R}_N] = [0.3, 0.7]^N$ the homogenisation problem (11) is solved with FE of uniform polynomial degree $p = 2$. The reference mesh is based on 80 nodes on the related reference composite interface $\mathcal{T}(\cdot; R_{\text{ref}})$ is shown in Figure 8. The computational mesh with composite interface $\mathcal{T}(\cdot, R)$ is then obtained by applying the transformation $\Psi(\cdot, R)$.

5.1 Surrogate validation

As a preparative step, we build an accelerated emulator in the tensor train format for $N = 6$ and $N = 12$ dimensional fuzzy input vectors $\tilde{R}_N$, yielding a compressed surrogate of the map $R \to \mathcal{H}(R)$.

Given $K = 15635$ $(N = 6)$ and $K = 12000 + 4096$ $(N = 12)$ samples that are normalised with respect to the sample mean and variance, we iteratively apply Algorithm 1 and Algorithm 2 with tensorised Chebyshev polynomials up to degree 5 in each coordinate. More precisely, we train the initial tensor train surrogate with a degree of two. Next, a new tensor train for polynomial degree $\deg+1$ up to $\deg = 4$ is set to the last tensor approximation as initial guess instead of starting with a random rank-1 tensor train. All tensor train component entries associated to the higher polynomial degree are initially set to zero. This training approach turn out to have two advantages. First, in the iterative procedure the training and validation sets are split randomly, resulting in a pseudo stochastic solver. A strategy that is successful in the context of machine learning. Second, there is a huge speed-up in the training procedure for finding a local minimum. In fact, with a naive tensor train training for $N = 12$ with initial tensor polynomial degree 5, we rarely observed convergence to meaningful surrogates given random initial values.

We use $\text{tol}_{\text{MSE}} = 1 \times 10^{-8}$, $\text{iter}_{\max} = 200$, $L_{\text{HIST}} = 10$, $\text{tol}_{\text{DECAY}} = 1 \times 10^{-5}$, $r_{\max} \leq 5, 7, 9, 20$ for $\deg = 2, \ldots, 5$, $r_{\text{add}} \in \{1, 2\}$, and $\delta = 1 \times 10^{-8}$. The results of the surrogate learning approach are depicted in Tables 1 and 2, which complement Figures 10 and 11, showing mean square error or pointwise relative and absolute errors. The highlighted entries in both tables show a pointwise lack of accuracy of the tensor train surrogate for the H_{13} and H_{23} components,

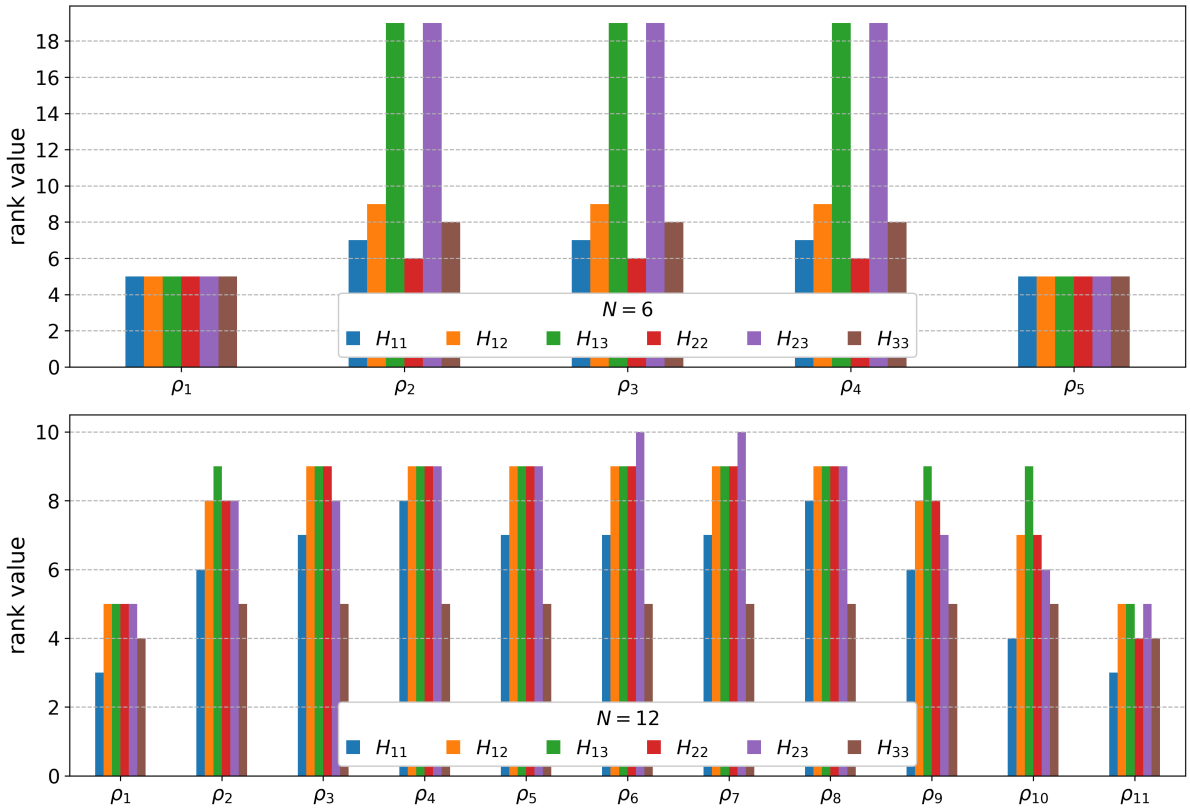

Figure 9: Final ranks of rank adaptive reconstruction of the tensor train surrogate for $N = 6$ (top) and $N = 12$ (bottom). In the algorithm, the maximum rank is limited to 20. The tensor train surrogate consists of Chebychev polynomials of degree 5 in each direction.

which represent the pure rotational or anisotropic contribution in the overall upscaled tensor $\mathcal{H}$ on the used test sets. Nevertheless, strikingly small mean squared errors can be observed as a result of the proposed optimization algorithm. Figures 10 and 11 display the value ranges of the subcomponents of $\mathcal{H}$ and the overall absolute and relative errors of the subcomponents and the full tensor $\mathcal{H}$. We observe that the reduced (pointwise) accuracy of the surrogates for H_{13} and H_{23} does not influence the overall error for the full parametric tensor $\mathcal{H}$. The final obtained ranks obtained with the rank adaptive algorithm are depicted in Figure 9 for $N = 6$ and $N = 12$.

5.2 Distances to the isotropy and orthotropy material class

In this section we apply the tensor train emulator to obtain an approximation of the parametric constitutive tensor $\mathcal{H}(R)$ of the effective material defined in (24), given an parametrisation of the inclusion through the vector $R \in C_0[\tilde{R}_{N,b}]$. For each constitutive tensor we compute the distance to the isotropy class, denoted by d_{iso}, and orthotropy class, denoted by d_{ortho}, according to (14). The fuzzy uncertainty of the boundary is propagated in terms of α-cuts. On each α-level, two optimization problems with constraints defined in (21) have to be solved, where $\mathcal{Q}$ is either d_{iso} or d_{ortho}. As optimiser we use a restarted trust region scheme to minimise the non-convex and non-linear target function with non-linear constraints.

Figure 12 shows the experimental results for $\mathcal{Q} = d_{\mathrm{iso}}$ with $N = 6$, zero α-cut $C_0[\tilde{R}_N] = [0.3, 0.7]^N$ and the total variation bounds $b = 0.5, 1, \infty$. We point out that since $D = [-1, 1]^2$ is not of special

Table 1: Surrogate validation for $N = 6$ on $[0.3, 0.7]^N$ based on 15635 data points randomly split into 14635 training and 1000 test samples. The highlighted values of maximum relative errors of H_{13} and H_{23} are the result of the surrogate model approximating a value 1×10^{-7} with 1×10^{-4}. These effects do not spoil the accuracy of the total surrogate $\mathcal{H}$ in subsequent experiments.

	validation set			training set
	MSE	max error	max rel. error	MSE
H_{11}	4.6×10^{-9}	2.9×10^{-1}	2.1×10^{-4}	4.5×10^{-9}
H_{22}	10.2×10^{-9}	6.3×10^{-1}	6.0×10^{-4}	9.4×10^{-9}
H_{33}	9.3×10^{-9}	1.3×10^{-1}	3.2×10^{-4}	8.6×10^{-9}
H_{12}	9.1×10^{-9}	7.6×10^{-2}	3.1×10^{-4}	8.6×10^{-9}
H_{13}	88.8×10^{-9}	1.1×10^{-2}	$1.4 \times 10^{+3}$	43.7×10^{-9}
H_{23}	97.9×10^{-9}	9.7×10^{-3}	$1.2 \times 10^{+3}$	45.5×10^{-9}

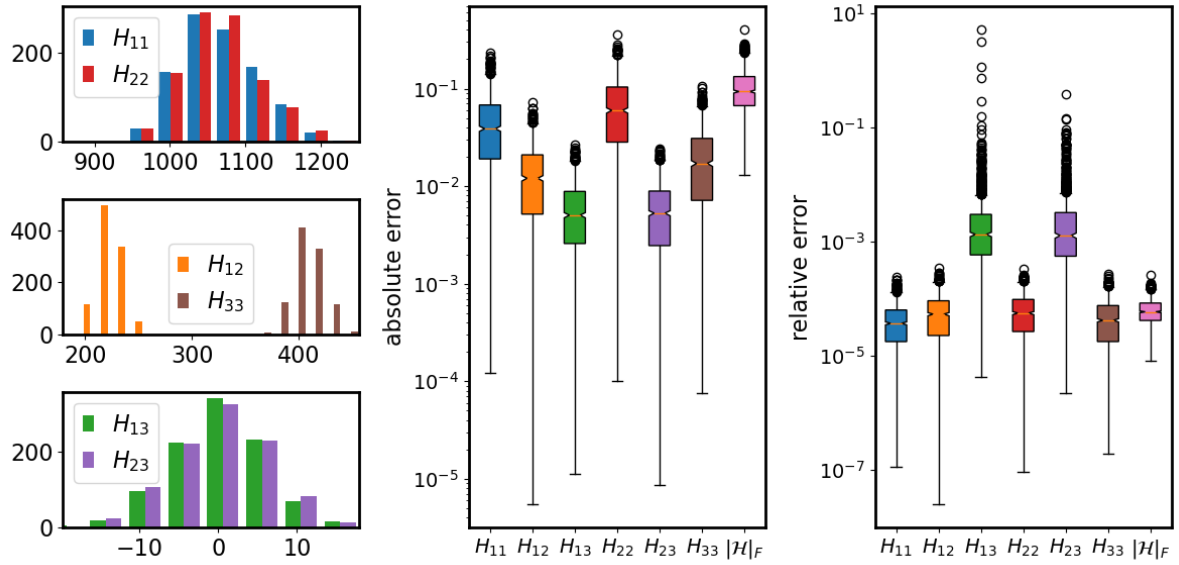

Figure 10: Validation of TT surrogate for $N = 6$ trained on $[0.3, 0.7]^6$. **Left**: value ranges of the subcomponents of $\mathcal{H}$, **Center**: pointwise absolute error on validation set, **Right**: pointwise relative error on validation set.

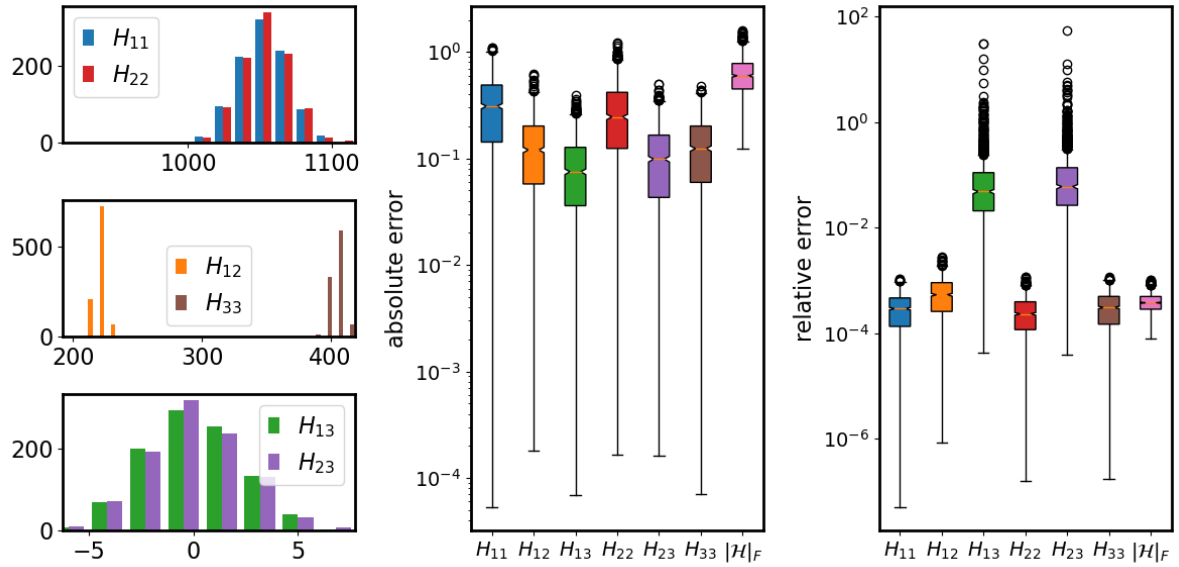

Figure 11: Validation of TT surrogate for $N = 12$ trained on $[0.4, 0.6]^{12}$. **Left**: value ranges of the subcomponents of $\mathcal{H}$, **Center**: pointwise absolute error on validation set, **Right**: pointwise relative error on validation set.

Table 2: Surrogate validation for $N = 12$ on $[0.4, 0.6]^N$ trained on normalised data. The mean squared error (MSE) is computed w.r.t. to the normalised value range of the data. The maximum pointwise relative and absolute errors are measured w.r.t to the surrogate values, which are shifted and scaled back to the original range. The highlighted values of maximum relative errors of H_{13} and H_{23} are the result of the surrogate model approximating a value 1×10^{-7} with 1×10^{-4}.

	validation set			training set
	MSE	max error	max rel. error	MSE
H_{11}	1.1×10^{-7}	3.5×10^{0}	3.1×10^{-3}	5.9×10^{-8}
H_{22}	1.0×10^{-7}	3.8×10^{0}	3.3×10^{-3}	7.4×10^{-8}
H_{33}	6.8×10^{-7}	5.1×10^{0}	1.2×10^{-2}	5.2×10^{-7}
H_{12}	5.1×10^{-7}	1.8×10^{0}	8.0×10^{-3}	3.0×10^{-7}
H_{13}	6.9×10^{-5}	0.8×10^{0}	$1.4 \times 10^{+4}$	4.4×10^{-5}
H_{23}	1.0×10^{-4}	0.6×10^{0}	$3.5 \times 10^{+3}$	7.5×10^{-5}

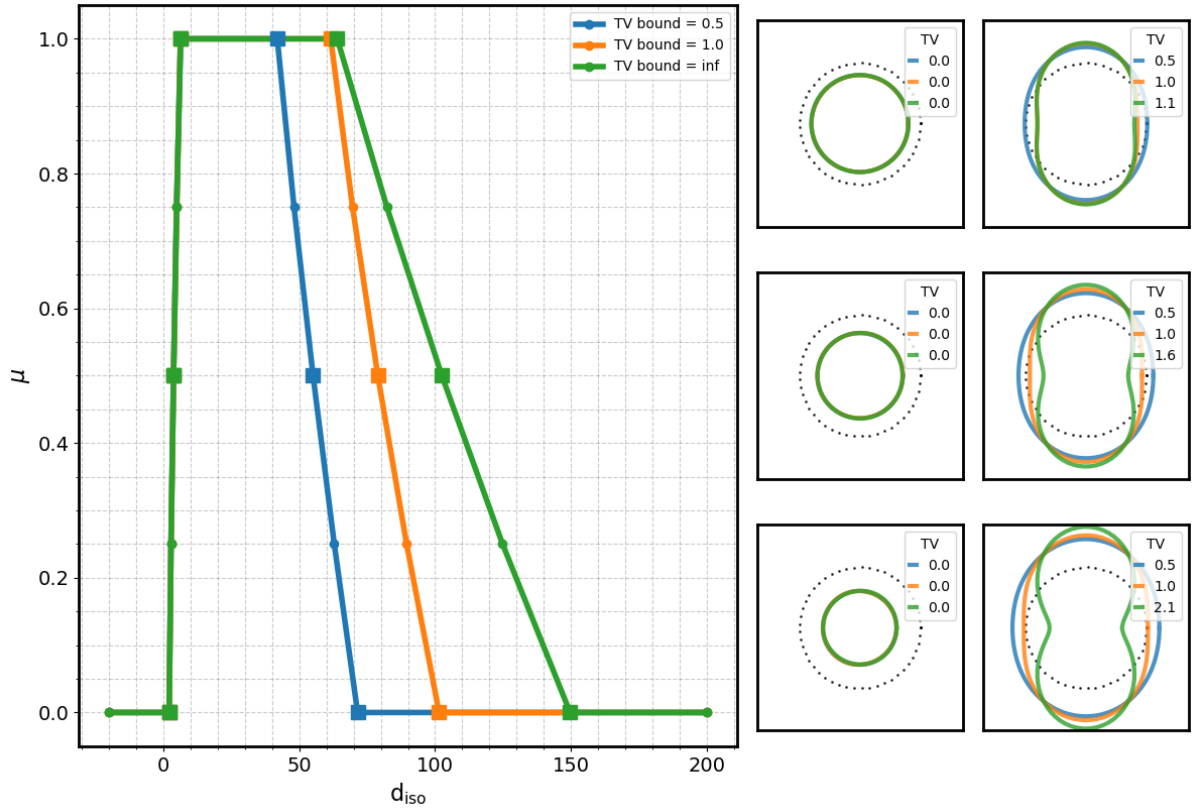

Figure 12: Fuzzy propagation: distance to isotropic material class represented by $\mathbb{E}\mathrm{la}(2, \mathrm{iso})$ based on different bounds $b = 0.5, 1, \infty$ for the total variation with $N = 6$. **Left:** membership function of $\tilde{\mathcal{Q}}_b$ for $\mathcal{Q} = \mathrm{d}_{\mathrm{iso}}$ with square markers bounding the alpha-cuts with $\alpha = 0., 0.5, 1.$ **Right:** underlying coloured shapes of the inclusions associated with the extremal points displayed as square markers with same colour along the membership function.

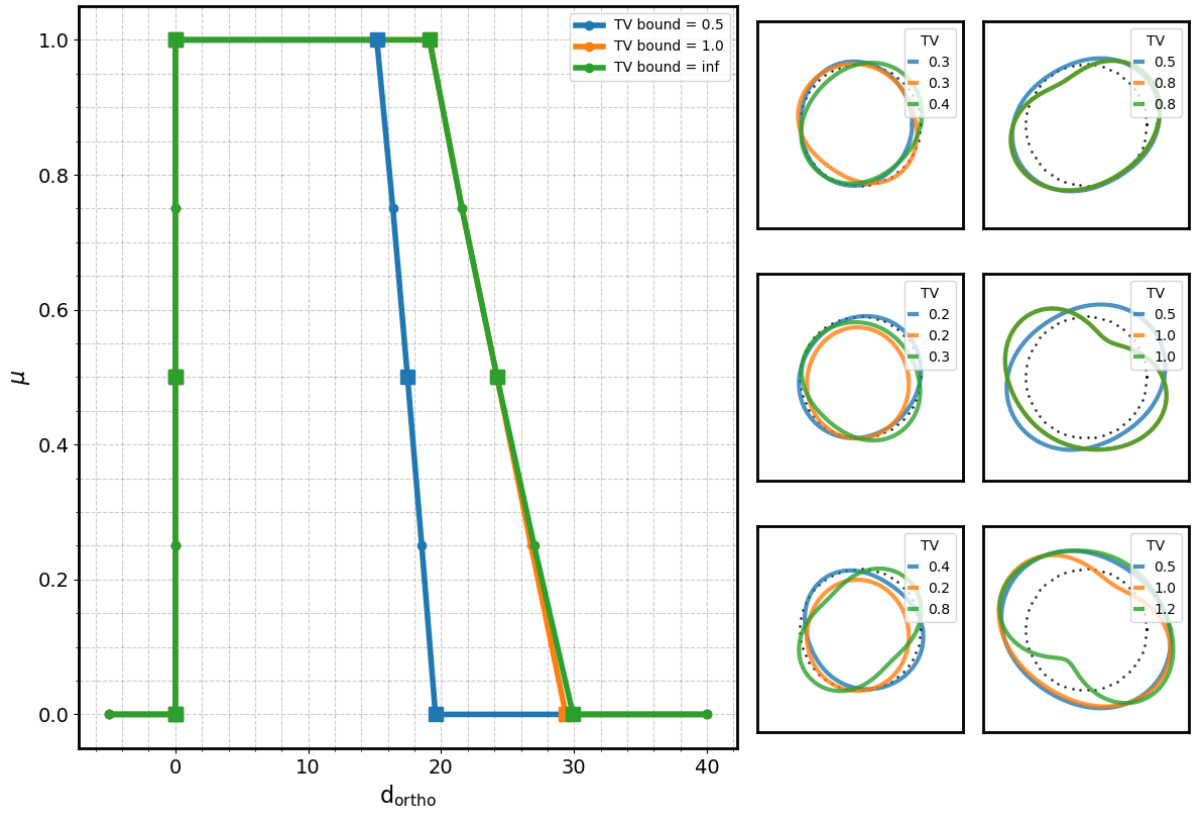

Figure 13: Fuzzy propagation: distance to the orthotropic material class represented by $\mathbb{E}\mathrm{la}(2, \mathrm{ortho})$ based on different bounds $b = 0.5, 1, \infty$ for the total variation with $N = 6$. **Left:** membership function of $\tilde{\mathcal{Q}}_b$ for $\mathcal{Q} = \mathrm{d}_{\mathrm{ortho}}$ with square markers bounding the alpha-cuts for $\alpha = 0., 0.5, 1.$ **Right:** underlying coloured shapes of the inclusions associated with the extremal points displayed as square markers with same colour along the membership function.

hexagonal shape but of square shape, a circular inclusion does not yield isotropic effective material properties. Nevertheless, the circular shape – while exhibiting vanishing total variation – provides effective properties closest to the isotropy class. Since in our experiments we choose a stiffer material as inclusion, the circular inclusion minimises its size proportional to the possible maximal radius encoded in the α-level. In this sense, the size of a circle is a measure of perturbation of the isotropic matrix material. Moreover, if the total variation and radii bounds allow it, the inclusion converges to a peanut shape. The green peanut shaped inclusion in Figure 12 marks the inclusion with maximum distance to the isotropic material class for the given parameterisation family $B_{N,\infty}$ from (18). Note that by rotational invariance also the peanut rotation of $\pi/2$ yields the same maximising shape.

Figure 14 pictures the result for $\mathcal{Q} = d_{\mathrm{iso}}$ with $N = 12$, zero α-cut $C_0[\tilde{R}_N] = [0.4, 0.6]^N$ and total variation bounds $b = 0.5, 1, \infty$. The shrinked domain has an immediate impact on the maximal possible total variation bound of all interface realisations. Consequently, maximum distances are caused by curves with similar shape up to rotation. Already for a total variation of 0.5, a symmetric shape emerges that becomes more prominent with increasing total variation.

Figure 13 depicts the experimental results for $\mathcal{Q} = d_{\mathrm{ortho}}$ with $N = 6$, zero α-cut $C_0[\tilde{R}_N] = [0.3, 0.7]^N$ and total variation bounds $b = 0.5, 1, \infty$. A minimum of 0 is attained on each alpha cut of the corresponding membership function, since the orthotropy class $\mathbb{E}\mathrm{la}(2, \mathrm{ortho})$ contains the square symmetric class. Many boundaries in $B_{N,b}$ lead to a shape that yields a square symmetric effective

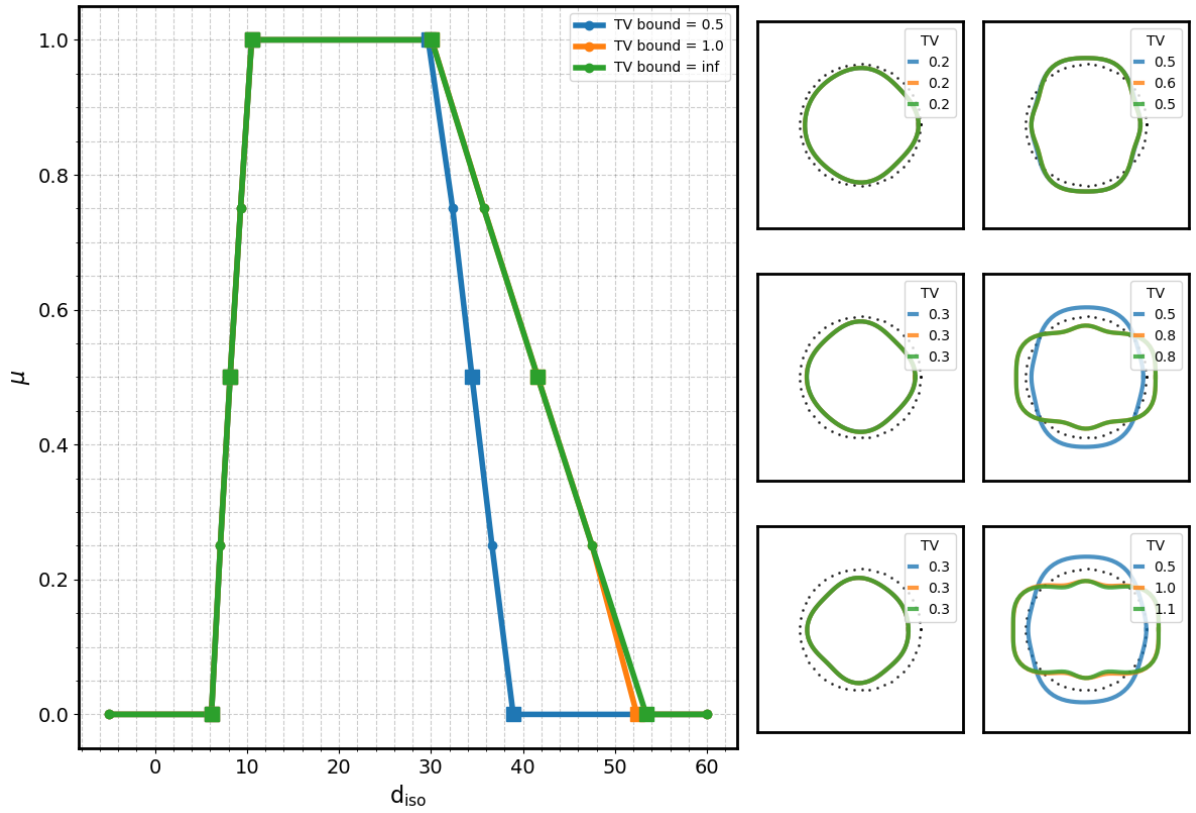

Figure 14: Fuzzy propagation: distance to the isotropic material class represented by $\mathbb{E}\mathrm{la}(2, \mathrm{iso})$ based on different bounds $b = 0.5, 1, \infty$ for the total variation with $N = 12$. **Left:** membership function of $\tilde{\mathcal{Q}}_b$ for $\mathcal{Q} = \mathrm{d}_{\mathrm{iso}}$ with square markers bounding the alpha-cuts for $\alpha = 0., 0.5, 1.$ **Right:** underlying coloured shapes of the inclusions associated with the extremal points displayed as square markers with same colour along the membership function.

material.

As typical maximiser of the distance to the orthotropy class, a bean shape is found. We observe that the maximal possible total variation value of $B_{N,b}$ is not exhausted when attaining the maximal distance. Note that due to rotational invariance, the bean shape can be rotated by multiples of $\pi/2$ while still being a (in fact the same) maximiser.

Figure 15 shows the experimental results for $\mathcal{Q} = d_{\mathrm{ortho}}$ with $N = 12$, zero α-cut $C_0[\tilde{R}_N] = [0.4, 0.6]^N$ and total variation bounds $b = 0.5, 1, \infty$. Again the shrinked domain has an immediate impact on the maximal possible total variation bound of all interface realisations. Consequently, maximum distances are attained by curves with similar shapes up to rotation. We observe that symmetric dented shape maximises the distance to the orthotropy class for the $\alpha = 1$ cut or a total variation smaller or equal to 0.5. However, as the total variation bound gets larger and we allow for larger fluctuations due to a wider parameter range the inclusion converges to a non-axis aligned structure with non-symmetric dented shape.

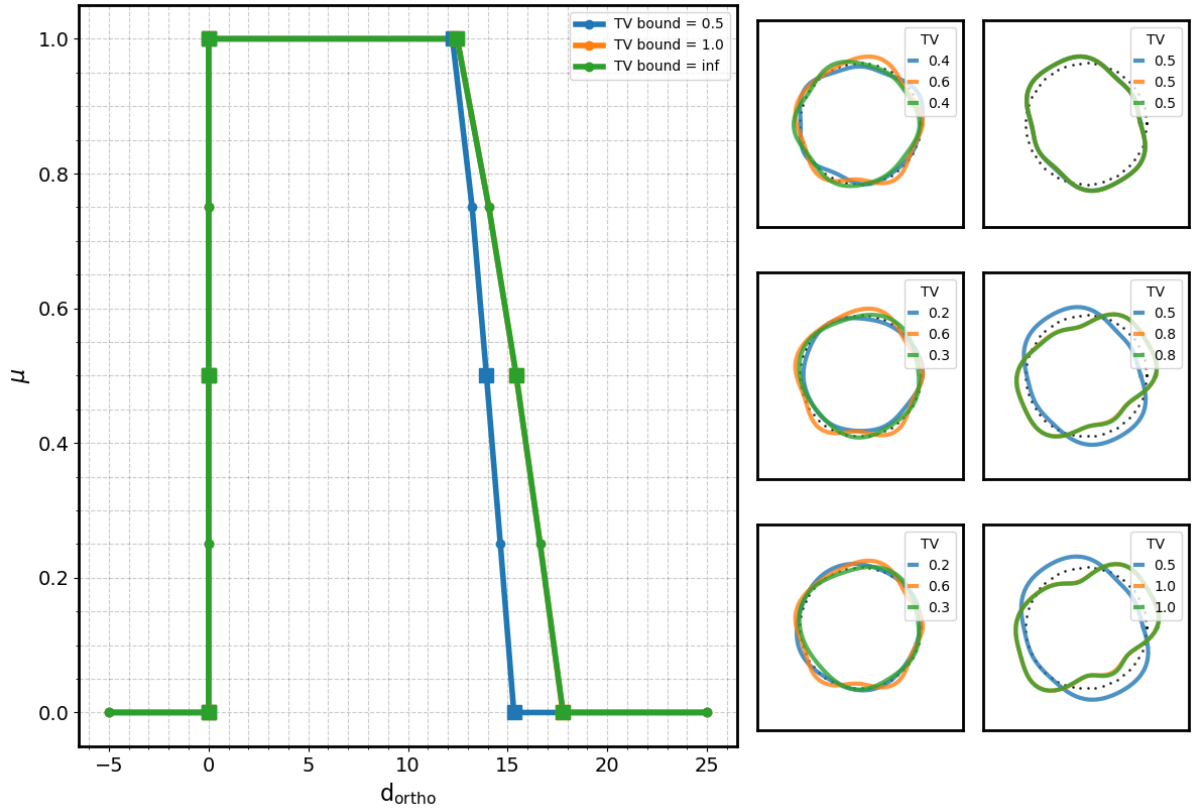

Figure 15: Fuzzy propagation: distance to the orthotropic material class represented by $\mathbb{E}\mathrm{la}(2, \mathrm{ortho})$ based on different bounds $b = 0.5, 1, \infty$ for the total variation with $N = 12$. **Left:** membership function of $\tilde{\mathcal{Q}}_b$ for $\mathcal{Q} = \mathrm{d}_{\mathrm{ortho}}$ with square markers bounding the alpha-cuts for $\alpha = 0., 0.5, 1.$ **Right:** underlying coloured shapes of the inclusions associated with the extremal points displayed as square markers with same colour along the membership function.

5.3 Best/worst case estimates for non-homogenised matrix composites

We consider the domain $D = [-N_s, N_s] \times [-N_s, N_s]$ with $N_s = 8$ and a checkerboard partitioning $D = \overline{\bigcup_{i,j} D_{ij}}$ with square subdomains D_{ij} defined by

$$D_{ij} := [-N_s + (i-1), -N_s + i] \times [-N_s + (j-1), -N_s + j] \quad \text{for } i, j = 1, \dots, N_s.$$

On each subdomain D_{ij} we consider a single two phase composite as defined by (23) using a local polar coordinate system w.r.t. the midpoint of D_{ij}, encoded in a material tensor $\boldsymbol{C}_{\text{inhomo}}$ with piecewise values $\boldsymbol{C}_{\text{incl}}$ and $\boldsymbol{C}_{\text{matrix}}$ specified in Section 5.1.

For this experiment we choose the non-interactive fuzzy set $\tilde{R}_{N,\infty}$ with $N = 6$ trapezoidal fuzzy components characterised by

$$\begin{aligned} C_0[\tilde{R}_{N,\infty}] &= [0.32, 0.63] \times [0.35, 0.66] \times [0.36, 0.70] \\ &\quad \times [0.32, 0.62] \times [0.38, 0.67] \times [0.31, 0.66] \\ C_1[\tilde{R}_{N,\infty}] &= [0.48, 0.55] \times [0.47, 0.56] \times [0.49, 0.55] \\ &\quad \times [0.47, 0.56] \times [0.45, 0.59] \times [0.48, 0.50]. \end{aligned}$$

In between these prescribed points, the α-levels are obtained by linear interpolation. The TV bound is ignored in this experiment.

Furthermore, we consider a homogenised material tensor $\boldsymbol{C}_{\text{homo}} = \mathcal{H}(R)$ for $R \in C_0[\tilde{R}_{N,b}]$ obtained from the homogenisation process of Sections 2.2 and 5.1. In each domain, we model individual star shaped material inclusions as in (23) with boundaries of uniformly bounded total variation smaller or equal to b.

Given a material law $\boldsymbol{C} \in \{\boldsymbol{C}_{\text{inhomo}}, \boldsymbol{C}_{\text{homo}}\}$, we then solve the linear elasticity problem

$$\left.\begin{aligned} \mathbf{0} &= -\operatorname{div} \boldsymbol{\sigma} && \text{equilibrium eq.} \\ \boldsymbol{\epsilon} &= \left[\nabla \boldsymbol{u} + \nabla^{\mathrm{T}} \boldsymbol{u}\right]/2 && \text{strain-displacement eq.} \\ \boldsymbol{\sigma} &= \boldsymbol{C} : \boldsymbol{\epsilon} && \text{constitutive eq.} \end{aligned}\right\} \text{ in } D, \qquad (29)$$

$$\begin{aligned} \boldsymbol{u} &= \mathbf{0} && \text{Dirichlet b.c.} && \text{on } \Gamma_{\mathbf{0}}, \\ \boldsymbol{\sigma} \cdot \boldsymbol{n} &= \boldsymbol{g} && \text{Neumann b.c.} && \text{on } \Gamma_{\boldsymbol{\sigma}}, \end{aligned}$$

representing a linear elastic tensile test. Here, $\Gamma_{\mathbf{0}} = \{-N_s\} \times [-N_s, N_s]$ and

$$\boldsymbol{g}(x) = \begin{cases} \mathbf{0}, & x \in [-N_s, N_s] \times \{-N_s, N_s\}, \\ 100\boldsymbol{e}_1, & x \in \{N_s\} \times [-N_s, N_s]. \end{cases} \qquad (30)$$

We are interested in the fuzzy propagation of the homogenised material through the average displacement $\mathcal{Q} = \overline{u}$ defined by

$$\overline{u} := \frac{1}{\operatorname{vol}(D)} \int_D \|\boldsymbol{u}(x)\|^2 \, \mathrm{d}x,$$

with the solution $\boldsymbol{u}$ of (29). Figure 16 shows the resulting membership function based on the fuzzy homogenised material law. The black dots mark resulting average displacements obtained for various non-periodic inclusions. Moreover, some configurations of possible realisations of the 8×8 inclusions are displayed. The corresponding average displacement is marked with colours, accordingly. Given any non-periodic configuration of prescribed matrix composites, we observe that the membership function at each α-level bounds the various average displacements. In particular, for $\alpha = 0., 0.5, 1$

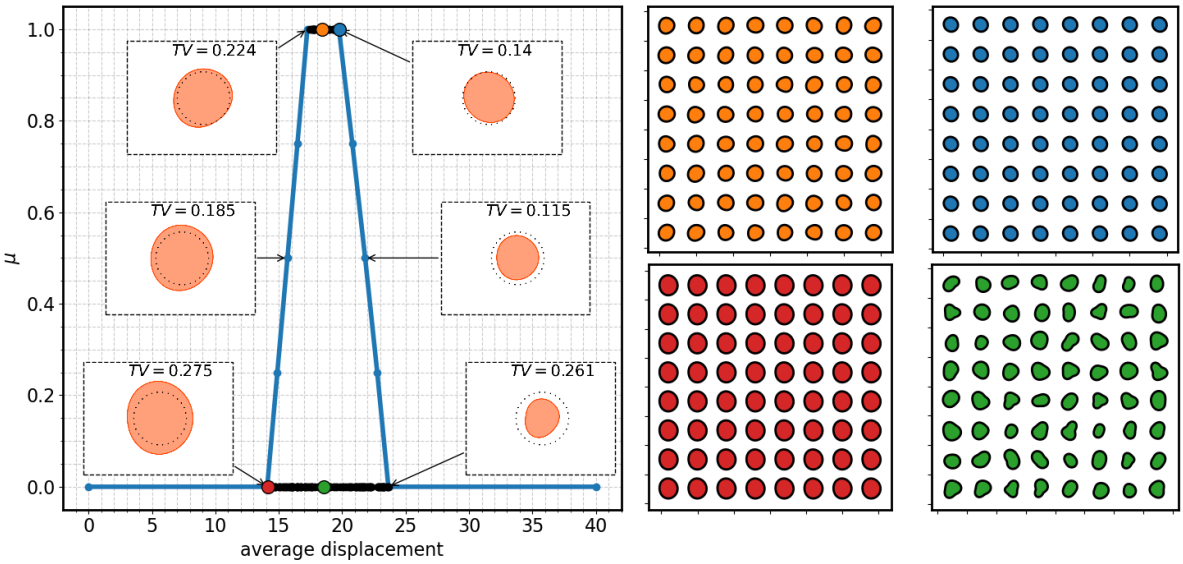

Figure 16: Fuzzy propagation: average displacement based on fuzzy homogenised material with $N = 6$. **Left**: resulting membership function with composite shapes causing the α-cut ranges in a periodic constellations in $\boldsymbol{C}_{\text{inhomo}}$. **Right**: various periodic (red and green) and non-periodic (blue and magenta) composite constellations yielding average displacements within the area of black dots.

we illustrated a corresponding single composite shape that (assumed in a periodic structure) results in the minimum and maximum average displacements. As the interior composite is slightly stiffer than the surrounding matrix material, it is to be expected that the shapes of the minimiser and maximiser attempt to exhaust or avoid the maximum capacity of the parameter range encoded in $C_\alpha[\tilde{R}_{N,\infty}]$. It is noteworthy that the homogenised material is able to serve as worst/best case estimator for this particular quantity of interest (i.e. the average displacement). As long as the repetition of the same cell leads to extremal values of the quantity of interest, the fuzzy homogenised material functions as a worst/best case estimator.

6 Conclusion

We considered the possibilistic shape uncertainty of one inclusion induced by a blurred image. In this setting, computational stochastic homogenisation was carried out to propagate the uncertainty through the linear elasticity model, resulting in a fuzzy effective material. Eventually, the effective material was examined with respect to its distance to the orthotropic/isotropic material class. Moreover, it was used as a worst/best case estimator with respect to the global average displacement for a non-homogenised material.

To achieve this result, two major obstacles had to be overcome. The first was caused by the discontinuous mapping from boundary to effective material, which was a consequence of the automatic re-meshing for each new boundary instance. This was successfully resolved with an arbitrarily smooth transformation of a single reference mesh onto the respective mesh for a domain with a star-shaped inclusion. The second challenge was given by the computational effort needed to perform the (possibilistic) uncertainty propagation. Depending on the optimiser and the quantity of interest at hand, each α-cut required up to 5×10^4 computational homogenisation simulations. This problem was successfully resolved with a highly accurate tensor train emulator.

We provide an (numerical) analysis for a problem where only little knowledge is given and only simple assumptions can be made. This may be distinguished from other works, where more prior knowledge is given and more elaborated assumptions are suitable. In the latter scenario, one usually can utilise the Bayesian framework to model the uncertainty, see [47, 59], where in our scenario stochastic modelling may lead to a false confidence [6]. While usually the uncertainty of material properties is modelled with precise probabilities, leading to statements about expectation values and probabilities of failure, cf. [14, 62], we model geometrical uncertainties with imprecise probability, leading to statements about possible intervals and worst/best case configurations. Even if an imprecise probability approach for geometrical uncertainty is chosen, the geometrical shape is often restricted to simple parametrisations like a circle of varying diameter [49]. This in fact is a very useful simplification, for instance if the observed quantities only depend on the volume ratio of the two materials. Nonetheless, our experiments demonstrate that the shape determines if the effective material is isotropic, orthotropic or anisotropic. A circle always results in an orthotropic effective material in the considered case with unit square cells. Furthermore, our tensor train surrogate shows a remarkable accuracy of a relative error of order $\mathcal{O}(10^{-4})$. This is partly the result of a suitable choice of features, the novel rank-adaptive training strategy and the continuity induced by using a mesh transformation instead of automatic re-meshing. Compared to other works such as [48, 57], where standard generic methods like artificial neural networks and polynomial chaos are used in a similar context, we gain several orders of accuracy.

To focus on the influence of the shape uncertainty, other parts in our setting and analysis were kept simple. These parts are ideal starting points for future research. The homogenisation, for example, was performed with two phases of linear elastic materials. This can easily be substituted with more sophisticated materials – one may think of anisotropy, damage and higher contrast – or different homogenisation settings. The assumption of a star-shaped inclusion can be discarded with an adjusted edge detection and a different parametrisation of the boundary. Furthermore, the roughness measurement via total variation can be exchanged or extended with other restrictions of the boundary curves. In addition, it is possible to model the material constants appropriately with precise probabilities. By doing so, we add a stochastic dimension which together with the possibilistic uncertainty results in a *fuzzy-stochastic* model.

Finally, we hope that our presented contributions, namely the treatment of discontinuity from remeshing, the fuzzy edge detection, and the highly accurate tensor train surrogate, can be used and extended beneficially in other research to simulate composite materials in the presence of shape uncertainty.

Acknowledgements

The authors gratefully acknowledge the financial support of the German Research Foundation (DFG) within the Subproject 4 and 10 of the Priority Programme "Polymorphic uncertainty modelling for the numerical design of structures – SPP 1886".

References

[1] Arnaud Anantharaman and Claude Le Bris. Elements of mathematical foundations for numerical approaches for weakly random homogenization problems. *Communications in Computational*

Physics, 11(4):1103–1143, 2012.

[2] Adrien Antonelli, Boris Desmorat, Boris Kolev, and Rodrigue Desmorat. Distance to plane elasticity orthotropy by euler-lagrange method. *arXiv preprint arXiv:2107.14456*, 2021.

[3] Ivo Babuška. Homogenization approach in engineering. In *Computing methods in applied sciences and engineering*, pages 137–153. Springer, 1976.

[4] Ivo Babuška, Börje Andersson, Paul J Smith, and Klas Levin. Damage analysis of fiber composites part i: Statistical analysis on fiber scale. *Computer Methods in Applied Mechanics and Engineering*, 172(1-4):27–77, 1999.

[5] Ivo Babuška and Mohammad Motamed. A fuzzy-stochastic multiscale model for fiber composites: A one-dimensional study. *Computer Methods in Applied Mechanics and Engineering*, 302:109–130, 2016.

[6] Michael Scott Balch, Ryan Martin, and Scott Ferson. Satellite conjunction analysis and the false confidence theorem. *Proceedings of the Royal Society A*, 475(2227):20180565, 2019.

[7] Xavier Blanc, Claude Le Bris, and P-L Lions. Stochastic homogenization and random lattices. *Journal de mathématiques pures et appliquées*, 88(1):34–63, 2007.

[8] Alain Bourgeat and Andrey Piatnitski. Approximations of effective coefficients in stochastic homogenization. In *Annales de l'IHP Probabilités et statistiques*, volume 40, pages 153–165, 2004.

[9] Claude Boutin. Homogenization Methods and Generalized Continua in Linear Elasticity. In *Altenbach H., Oechsner A.(eds) Encyclopedia of Continuum Mechanics.* Springer, 2019.

[10] Andrea Braides et al. *Gamma-convergence for Beginners*, volume 22. Clarendon Press, 2002.

[11] Michael Cannon. Blind deconvolution of spatially invariant image blurs with phase. *IEEE Transactions on Acoustics, Speech, and Signal Processing*, 24(1):58–63, 1976.

[12] Riccardo Casati and Maurizio Vedani. Metal matrix composites reinforced by nano-particles—a review. *Metals*, 4(1):65–83, 2014.

[13] Richard M Christensen. *Mechanics of composite materials*. Courier Corporation, 2012.

[14] Nikolay Dimitrov, Peter Friis-Hansen, and Christian Berggreen. Reliability analysis of a composite wind turbine blade section using the model correction factor method: Numerical study and validation. *Applied Composite Materials*, 20(1):17–39, 2013.

[15] Martin Drieschner, Hermann G Matthies, Truong-Vinh Hoang, Bojana V Rosić, Tim Ricken, Carla Henning, Georg-Peter Ostermeyer, Michael Müller, Stephan Brumme, Tarin Srisupattarawanit, et al. Analysis of polymorphic data uncertainties in engineering applications. *GAMM-Mitteilungen*, 42(2):e201900010, 2019.

[16] Martin Drieschner and Yuri Petryna. Acquisition of polymorphic uncertain data based on computer tomographic scans and integration in numerical models of adhesive bonds. *Preprint-Reihe des Fachgebiets Statik und Dynamik, Technische Universität Berlin*, 2019.

[17] Martin Eigel, Robert Gruhlke, Manuel Marschall, Philipp Trunschke, and Elmar Zander. ALEA - A Python Framework for Spectral Methods and Low-Rank Approximations in Uncertainty Quantification.

[18] Björn Engquist and Olof Runborg. Wavelet-based numerical homogenization with applications. In *Multiscale and multiresolution methods*, pages 97–148. Springer, 2002.

[19] Björn Engquist and Panagiotis E Souganidis. Asymptotic and numerical homogenization. *Acta Numerica*, 17:147–190, 2008.

[20] FEniCS Project - Automated solution of Differential Equations by the Finite Element Method.

[21] Christophe Geuzaine and Jean-François Remacle. Gmsh: A 3-d finite element mesh generator with built-in pre-and post-processing facilities. *International journal for numerical methods in engineering*, 79(11):1309–1331, 2009.

[22] Antoine Gloria, Stefan Neukamm, and Felix Otto. An optimal quantitative two-scale expansion in stochastic homogenization of discrete elliptic equations. *ESAIM: Mathematical Modelling and Numerical Analysis*, 48(2):325–346, 2014.

[23] Robert Gruhlke and Till Schäfer. Bubbles - A Python Framework for composite modelling.

[24] Robert Gruhlke and David Sommer. TensorTrain - A Python Framework for Tensor Train approximations with PyTorch and NumPy backend.

[25] Sebastian Holtz, Thorsten Rohwedder, and Reinhold Schneider. The alternating linear scheme for tensor optimization in the tensor train format. *SIAM Journal on Scientific Computing*, 34(2):A683–A713, 2012.

[26] Bobby R Hunt. The application of constrained least squares estimation to image restoration by digital computer. *IEEE Transactions on Computers*, 100(9):805–812, 1973.

[27] Robert M Jones. *Mechanics of composite materials (2nd ed.)*. CRC press, 2018.

[28] Deepa Kundur and Dimitrios Hatzinakos. Blind image deconvolution. *IEEE signal processing magazine*, 13(3):43–64, 1996.

[29] Pierre Ladeveze and Anthony Nouy. On a multiscale computational strategy with time and space homogenization for structural mechanics. *Computer Methods in Applied Mechanics and Engineering*, 192(28-30):3061–3087, 2003.

[30] Edmund Y Lam and Joseph W Goodman. Iterative statistical approach to blind image deconvolution. *JOSA A*, 17(7):1177–1184, 2000.

[31] Claude Le Bris, Frédéric Legoll, and William Minvielle. Special quasirandom structures: a selection approach for stochastic homogenization. *Monte Carlo Methods and Applications*, 22(1):25–54, 2016.

[32] Anat Levin, Yair Weiss, Fredo Durand, and William T Freeman. Understanding blind deconvolution algorithms. *IEEE transactions on pattern analysis and machine intelligence*, 33(12):2354–2367, 2011.

[33] Jean Mandel. Généralisation de la théorie de plasticité de wt koiter. *International Journal of Solids and structures*, 1(3):273–295, 1965.

[34] Georges Matheron. *Random sets and integral geometry*. Wiley New York, 1974.

[35] Keith Miller. Least squares methods for ill-posed problems with a prescribed bound. *SIAM Journal on Mathematical Analysis*, 1(1):52–74, 1970.

[36] David Moens and Michael Hanss. Non-probabilistic finite element analysis for parametric uncertainty treatment in applied mechanics: Recent advances. *Finite Elements in Analysis and Design*, 47(1):4–16, 2011.

[37] Bernd Möller and Michael Beer. Engineering computation under uncertainty–capabilities of non-traditional models. *Computers & Structures*, 86(10):1024–1041, 2008.

[38] Bernd Möller, Wolfgang Graf, Michael Beer, and Jan-Uwe Sickert. Fuzzy randomness-towards a new modeling of uncertainty. In *Fifth World Congress on Computational Mechanics, Vienna, Austria*, 2002.

[39] Fanny Moravec and Sophie Roman. Numerical computing of elastic homogenized coefficients for periodic fibrous tissue. *Applied and Computational Mechanics*, 3:141–152, 2009.

[40] Hung T Nguyen. A note on the extension principle for fuzzy sets. *Journal of Mathematical Analysis and Applications*, 64(2):369–380, 1978.

[41] Kristiina Oksman Niska and Mohini Sain. *Wood-polymer composites*. Woodhead Publishing Materials, 2008.

[42] Ivan V Oseledets. Tensor-train decomposition. *SIAM Journal on Scientific Computing*, 33(5):2295–2317, 2011.

[43] Martin Ostoja-Starzewski. Material spatial randomness: From statistical to representative volume element. *Probabilistic engineering mechanics*, 21(2):112–132, 2006.

[44] Martin Ostoja-Starzewski and J Schulte. Bounding of effective thermal conductivities of multiscale materials by essential and natural boundary conditions. *Physical review B*, 54(1):278, 1996.

[45] Houman Owhadi, Clint Scovel, Timothy John Sullivan, Mike McKerns, and Michael Ortiz. Optimal uncertainty quantification. *Siam Review*, 55(2):271–345, 2013.

[46] Scott Pecullan, LV Gibiansky, and Salvatore Torquato. Scale effects on the elastic behavior of periodic and hierarchical two-dimensional composites. *Journal of the Mechanics and Physics of Solids*, 47(7):1509–1542, 1999.

[47] Tishun Peng, Abhinav Saxena, Kai Goebel, Yibing Xiang, Shankar Sankararaman, and Yongming Liu. A novel bayesian imaging method for probabilistic delamination detection of composite materials. *Smart materials and structures*, 22(12):125019, 2013.

[48] Ghanshyam Pilania, Chenchen Wang, Xun Jiang, Sanguthevar Rajasekaran, and Ramamurthy Ramprasad. Accelerating materials property predictions using machine learning. *Scientific reports*, 3(1):1–6, 2013.

[49] Dmytro Pivovarov and Paul Steinmann. Modified sfem for computational homogenization of heterogeneous materials with microstructural geometric uncertainties. *Computational Mechanics*, 57(1):123–147, 2016.

[50] Pablo Ruiz, Xu Zhou, Javier Mateos, Rafael Molina, and Aggelos K Katsaggelos. Variational bayesian blind image deconvolution: A review. *Digital Signal Processing*, 47:116–127, 2015.

[51] Enrique Sánchez-Palencia. Non-homogeneous media and vibration theory. *Lecture notes in physics*, 127, 1980.

[52] M Ozgur Seydibeyoglu, Amar K Mohanty, and Manjusri Misra. *Fiber technology for fiber-reinforced composites*. Woodhead Publishing, 2017.

[53] Glenn Shafer. *A mathematical theory of evidence*, volume 42. Princeton university press, 1976.

[54] Man Mohan Sondhi. Image restoration: The removal of spatially invariant degradations. *Proceedings of the IEEE*, 60(7):842–853, 1972.

[55] Bastien Tranquart, Pierre Ladevèze, Emmanuel Baranger, and Anne Mouret. A computational approach for handling complex composite microstructures. *Composite Structures*, 94(6):2097–2109, 2012.

[56] Valery V Vasiliev and Evgeny V Morozov. *Advanced mechanics of composite materials and structures*. Elsevier, 2018.

[57] Maria Vasilyeva and Aleksey Tyrylgin. Machine learning for accelerating macroscopic parameters prediction for poroelasticity problem in stochastic media. *Computers & Mathematics with Applications*, 84:185–202, 2021.

[58] Pauli Virtanen, Ralf Gommers, Travis E. Oliphant, Matt Haberland, Tyler Reddy, David Cournapeau, Evgeni Burovski, Pearu Peterson, Warren Weckesser, Jonathan Bright, Stéfan J. van der Walt, Matthew Brett, Joshua Wilson, K. Jarrod Millman, Nikolay Mayorov, Andrew R. J. Nelson, Eric Jones, Robert Kern, Eric Larson, C J Carey, İlhan Polat, Yu Feng, Eric W. Moore, Jake VanderPlas, Denis Laxalde, Josef Perktold, Robert Cimrman, Ian Henriksen, E. A. Quintero, Charles R. Harris, Anne M. Archibald, Antônio H. Ribeiro, Fabian Pedregosa, Paul van Mulbregt, and SciPy 1.0 Contributors. SciPy 1.0: Fundamental Algorithms for Scientific Computing in Python. *Nature Methods*, 17:261–272, 2020.

[59] Gang Yan, Hao Sun, and Oral Büyüköztürk. Impact load identification for composite structures using bayesian regularization and unscented kalman filter. *Structural Control and Health Monitoring*, 24(5):e1910, 2017.

[60] Lotfi Asker Zadeh. The concept of a linguistic variable and its application to approximate reasoning I. *Information sciences*, 8(3):199–249, 1975.

[61] Lotfi Asker Zadeh. Fuzzy sets as a basis for a theory of possibility. *Fuzzy sets and systems*, 1(1):3–28, 1978.

[62] Xiaoyi Zhou, Peter Gosling, Zahur Ullah, Chris Pearce, et al. Exploiting the benefits of multi-scale analysis in reliability analysis for composite structures. *Composite Structures*, 155:197–212, 2016.